Tailoring of the magneto-transport properties, half-metallicity and vacancy-induced structural disorder in Co2ZrSn for spintronics

Journal of Alloys and Compounds 1027 (2025) 180557

Contents lists available at ScienceDirect

Journal of Alloys and Compounds

journal homepage: www.elsevier.com/locate/jalcom

Tailoring of the magneto-transport properties, half-metallicity and vacancy-induced structural disorder in Co_2ZrSn for spintronics

Alessandro Difalco [a,1], Alberto Castellero [a,b,*,2], Mauro Palumbo [a,3], Marcello Baricco [a,4], Stefano Boldrini [b,5], Alberto Ferrario [b,6], Carlo Fanciulli [c,7], Olivier Rouleau [d], Benjamin Villeroy [d], Gabriele Barrera [e,8], Paola Maria Tiberto [e,9], Paolo Allia [e,10], Eric Alleno [d,11]

[a] Dipartimento di Chimica and NIS-INSTM, Università di Torino, Via P. Giuria 7, Torino, Italy
[b] CNR-ICMATE, Corso Stati Uniti 4, Padova, Italy
[c] CNR-ICMATE, Via Gaetano Previati 1/E, Lecco, Italy
[d] Université Paris Est Creteil, CNRS, ICMPE, UMR 7182, 2-8, Rue H. Dunant, Thiais F-94320, France
[e] INRIM – Istituto Nazionale di Ricerca Metrologica, Strada delle Cacce 91, Torino, Italy

ARTICLE INFO

Keywords:
Heusler
Defects
Magnetic properties
Transport properties
Half-metallicity
DFT

ABSTRACT

In spintronics, the ability of half-metallic ferromagnets (HMF) to achieve 100 % spin-polarization is essential to develop next-generation magnetic tunnel-junctions. In this work, the effect of Co-vacancy point-defects on the half metallicity and magneto-transport properties of the promising Co_2ZrSn Heusler alloy are studied. The alloy is synthesized via several processing routes, involving different cooling rates and degrees of metastability. Polycrystalline samples are analyzed by synchrotron X-ray diffraction. The occupancy and the disorder of Co-sites in the crystal structure, evaluated by Rietveld refinement, are responsible for significant changes in such properties, such as the shrinking of the half-metallic band-gap, reduction of saturation magnetization and electrical conductivity. The electrical resistivity, R, measured at low temperature (below 300 K) show a change of regime from a T^2 to a T^α dependency, which is interpreted as a change of electron scattering mechanisms due to a crossover from a half-metallic to an itinerant ferromagnetic state. The thermoelectric figure of merit zT is here experimentally determined for the first time. Ab-initio calculated properties, both on pristine and defective structures, are in quantitative agreement with experiments and linearly scale with the Co-site occupancy, which does not affect the half-metallic ground state. Lastly, phonon and thermal properties are discussed in the framework of Slack's model..

1. Introduction

Since the generation and transport of spin-currents is considered decisive for the development of magnetic tunnel-junctions [1–4], half-metallic materials have recently attracted considerable attention for applications in spintronics and spin-caloritronics [5–9]. In this regard, the interest for half-metallic ferromagnets (HMF) is twofold. On the one hand, materials able to exhibit room temperature

* Corresponding author at: Dipartimento di Chimica and NIS-INSTM, Università di Torino, Via P. Giuria 7, Torino, Italy.
E-mail address: alberto.castellero@unito.it (A. Castellero).
[1] 0000-0003-4040-2832
[2] 0000-0001-8290-7543
[3] 0000-0002-0689-0839
[4] 0000-0002-2856-9894
[5] 0000-0002-2241-9748
[6] 0000-0002-0994-4919
[7] 0000-0003-4436-0385
[8] 0000-0002-3174-8092
[9] 0000-0002-7409-2281
[10] 0000-0002-9132-1701
[11] 0000-0003-0175-9783

https://doi.org/10.1016/j.jallcom.2025.180557
Received 13 December 2024; Received in revised form 24 March 2025; Accepted 20 April 2025
Available online 21 April 2025

half-metallicity are greatly looked after, as they are expected to show large spin-polarization, as well as high values of giant and tunnel magnetoresistance [1]. On the other hand, their ability to give rise to spin-Seebeck effects is also considered to be an effective way to generate and carry spin-currents even over relatively long distances [10]. Thus, they are deemed to be crucial for the development of spin-voltage generators [11].

As far as the magnetic properties of HMF are concerned, in spin-valves and magnetic tunnel-junctions, a pinned ferromagnetic layer (PL) is separated from a second ferromagnetic free layer (FL) by a spacer barrier. Depending on the relative magnetizations of PL and FL, these devices can exhibit a high-resistance state, when the magnetization of the layers is antiparallel, or a low resistance state, if their magnetization is parallel. The relative difference of resistance between these two states is called MR ratio, which is:

$$MR\ ratio = \frac{R_{ap} - R_p}{R_p} \tag{1}$$

where R_{ap} and R_p are the resistances of the system in the antiparallel and parallel states, respectively. According to the Julliere model [12,13], Eq. 1 can be written also in terms of the spin-polarization degrees, P_1 and P_2, exhibited by the two ferromagnetic layers, as:

$$MR\ ratio = \frac{2P_1P_2}{1 - P_1P_2} \tag{2}$$

From Eq. 2 it is possible to note that the MR ratio is infinite if both P_1 and P_2 are equal to 1, meaning that the device would be able to switch between a state of zero and infinite resistance. [14] This is the ultimate goal for such technology, and it is expected to be theoretically possible for half-metallic ferromagnets, in which the polarization of conduction electrons is predicted to be 100 % [1,14].

Concerning the transport properties of HMF materials, in 2014 Boona et al. [7] described the spin-dependent Seebeck effect as the result of the spin-dependence of the electronic density of states in ferromagnetic materials, where each spin component (up and down) give rise to a separate thermopower contribution (S_{up}, and S_{down}). According to the Stoner model, being the two spin-populations mutually independent, each population will have independent internal conductance and will form separate conduction channels (G_{up} and G_{down}). If a thermal gradient ΔT is imposed, the total current density j created by the thermal voltage inside the material is obtained by considering the two spin channels as two voltage generators connected in parallel, being ultimately the sum of two different terms, j_{up} and j_{down}, or $j_{up(down)} = G_{up(down)}S\Delta T$ (with S the Seebeck coefficient). If zero-current density conditions are imposed ($j = 0$), the resulting spin accumulation which will occur at the edges of the material (and that will decay over the spin-scattering diffusion length) is the spin-dependent Seebeck effect. This is the result of the imbalance between the number of spin-up and spin-down electrons displaced from their equilibrium state when a temperature gradient is imposed, and represents the spin accumulation density caused by such gradient. The spin-injection process occurs when a non-magnetic (NM) layer is positioned in contact with a ferromagnetic (FM) spin-voltage generator. In this configuration, the NM material will act as a spin-sink, and the accumulated spin-voltage will result in a polarized spin-current (inside the limits of the spin diffusion length of the material). Although the presence of a FM/NM interface is not a necessary condition for the occurrence of spin-dependent Seebeck effect, it is within this layered configuration that thermal spin-injection found the majority of scientific interest [1,7]. Beside magnetoresistance, the interest for HMF materials is also associated with the spin-transfer torque (STT) effect [15], which is used in spin-valves and in magnetic tunnel-junctions to generate a torque on magnetization, allowing to switch a memory cell value between “0” and “1” binary digits [9,16]. HMF compounds able to show spin-Seebeck effects [17–19] are considered as well promising in the field of spin-injection technologies and spin-voltage generators.

In this context, full-Heusler alloys (from now on named simply as Heusler alloys), which are ternary compounds with X_2YZ stoichiometry (where, X, Y are transition metals, and Z is a p-group element) and $L2_1$ crystal structure, are known for their peculiar magnetic [20] and thermoelectric properties [21]. Among these, Co-based Heusler compounds are considered to be the most promising candidates to achieve half-metallicity at room temperature as they combine high Curie temperature (T_C), relatively large band gaps in the minority-spin sub-band, good-enough Seebeck coefficients and electrical conductivities, and great lattice matching with a large variety of substrates [1]. Evidence of half-metallicity was collected for a large number of Co-based Heusler alloys such as Co_2FeSi [22], $Co_2FeAl_{0.5}Si_{0.5}$ [23], Co_2CrAl [24], Co_2MnSi [25], $Co_2V(Al,Ga)$ [26,27], $Co_2Ti(Si,Ge,Sn)$ [28], Co_2ZrSn [29,30], Co_2HfSn [30–32], and many others [33].

Concerning Co_2ZrSn, the electronic transport properties were reported in a previous work from room temperature up to 773 K [34]. The trends of Seebeck coefficient (S) and electrical conductivity (σ) as a function of temperature (T) were found to be peculiar and highly linked to T_C. In fact, the first (which was reported to be negative, indicating an n-type material) was found to increase linearly in absolute value from room T to T_C; whereas, above T_C, the value of S sets in a plateau around $-34\ \mu V\ K^{-1}$. The latter was instead measured to decrease linearly as a function of T below T_C, showing metallic-like behavior, where a change of regime occurred and σ started to linearly increase with T, presenting a semiconductor-like trend. Considering the magnetic properties, Indirect evidence of half-metallicity in Co_2ZrSn were found by applying the Edwards-Wohlfarth model for itinerant magnetization (M) and by analyzing the dependency of M on T at low temperatures [30]. In particular, it was found that a change of regime from a $M \propto T^{3/2}$ Bloch-type to a $M \propto T^2$ Stoner-type behavior occurred around 70 K. This was associated, similarly to other Heusler alloys [35], to a change in spin-diffusion mechanisms due to a crossover from a half-metallic to an itinerant ferromagnetic state. Regarding the saturation magnetization at 2 K, as well as the lattice parameter, values in literature are extremely scattered, ranging between 1.34 and 2.00 μ_B/formula-unit (f.u.) [29,36–42]. Explanations for this inconsistent behavior were proposed by various studies [39,40,43], with a general agreement on the fact that the presence of crystalline point defects, Co vacancies in particular, is the main responsible for such dispersed results. Being the electronic properties of Co_2ZrSn mainly depend on Co atoms, as the density of states (DOS) of the compound at the Fermi level is dominated by the Co contribution [30], it is believed that defects involving Co-sites ordering play the major role on the modification of electronic, magnetic and half-metallicity of Co_2ZrSn and other Co-based Heusler compounds [1,34,39,43].

The aim of this work is to understand how the presence of Co vacancies, which are among the simplest and most diffuse defects involving Co-sites, affect the transport properties, magnetism and half-metallicity of Co_2ZrSn, providing quantitative results and defining trends. To achieve this, we synthesized the Co_2ZrSn compound with several processing routes, each involving different cooling rates and heat treatments. Since the cooling rate is responsible for the existence of various degrees of disorder and defect concentrations inside the Heusler structure [44,45], the use of various synthesis procedures allowed to obtain samples with diverse lattice ordering and Co-site occupancy. Specimens were prepared by arc-melting (As cast), arc-melting with subsequent annealing (Annealed), and rapid solidification (melt-spinning) followed by spark-plasma sintering (SPS). The Co-site occupancy and the relative disorder of the lattice structure were evaluated using two independent XRD-based model: the first based on Rietveld refinement, and the second on peaks intensities.

On the base of the transport (Seebeck coefficient, electrical conductivity, thermal conductivity, Hall coefficient, and zT), and magnetic characterization, we found a strong structure-properties correlation in Co_2ZrSn, which is reflected also in its half-metallicity. Ab-initio

calculations were also performed in a vacancy-defective supercell in order to compare the electronic properties with those of the pristine compound. The effect on lattice parameter of Zr and Sn anti-sites in the 8c site, as well as that of several other defects (swap, and off-stoichiometry), was also evaluated. Finally, the phonon band structure, phonon density of states, the elastic properties, as well as several other lattice-dependent thermal properties of the pristine material were calculated. Such results were analyzed in the framework of Slack's model of thermal conductivity, and later compared with the experimentally observed data.

2. Materials and methods

Elemental metals (Co 99.97 %, Zr 99.90 %, Sn 99.97 % purity) were weighted in the appropriate stoichiometric quantity and melted in an Edmund Buhler GmbH (Bodelshausen, Germany) arc-furnace several times to ensure homogeneity. Subsequently, a part of the so obtained as cast sample was wrapped in a Ta foil, sealed in an evacuated quartz tube, and annealed for 6 days at 1273 K. Another part of the as cast sample was re-melted inside a boron nitride crucible and injected onto a rotary copper wheel (20 m/s speed) using an Edmund Buhler melt-spinning apparatus. The rapidly-solidified sample was hand-grinded into powder and then sintered by spark plasma sintering (SPS) in a Fuji 515 S sinter machine, using graphite moulds lined with graphite paper. Several pellets with a diameter of 8–10 mm and thickness approximately of 2.5 mm were obtained under the optimal sintering conditions, which were found to be 1223 K as ceiling temperature kept for 1 minute (1.5 K/s as both heating and cooling rate), and 66 MPa of pressure. The specimens are labeled as follows:

- Arc melted Co_2ZrSn alloy starting from pure elements: As cast.
- As cast specimen annealed at 1273 K for 6 days: Annealed.
- Rapidly solidified Co_2ZrSn alloy obtained with melt-spinning technique: Melt-spun.
- Spark-plasma sintered Co_2ZrSn starting from pulverized Melt-spun sample: SPS.
- SPS specimen subsequently annealed at 1273 K for 6 days: SPS+An.

Samples were crushed into powder and analyzed by X-Ray Diffraction (XRD) at the Soleil synchrotron facility (91190 Saint-Aubin, France) with the CRISTAL beamline (wavelength 0.51341 Å) in the Debye-Scherrer geometry. The XRD analysis was also performed with a Cu-Kα laboratory-scale PANalytical X'Pert Pro diffractometer in the Bragg-Brentano geometry. The Rietveld refinement procedure was performed using the MAUD code [46]. Samples were polished down to 40 nm roughness and characterized with a TESCAN Vega 4 Scanning Electronic Microscope (SEM) equipped with an Oxford Instruments Energy Dispersion Spectroscopy (EDS) Ultim Max 40 probe. The Electron Backscattered Diffraction analysis (EBSD) was performed with a TESCAN S9000G Field-Emission SEM (FESEM) equipped with an Oxford Instruments Symmetry S3 EBSD probe. Samples density was measured with a distilled water pycnometer.

The Seebeck coefficient and electrical resistivity of the as cast, annealed and spark plasma sintered (SPS) samples were measured above room temperature on bar-shaped specimens using the instrumentations described in Ref. [47,48]. The Seebeeck coefficient below room temperature was characterized with a homemade equipment. Thermal diffusivities were collected by laser flash technique with Netzsch (Selb, Germany) 427 and 457 analyzers; whereas, heat capacities were tested on a Perkin Elmer (Waltham, MA, USA) DSC 8000 calorimeter. The electrical resistivity and Hall coefficients below room temperature were analyzed with a Quantum Design (Darmstadt, Germany) Physical Properties Measurement System, PPMS (DC mode, Van Der Pauw geometry), from 2 K to 300 K. In the latter case, the magnetic field was varied between 7 and −7 T. Static magnetic properties were measured with a Quantum Design MPMS3 SQUID magnetometer, and with the abovementioned PPMS system, in the magnetic field interval of 0 ± 7 T. For higher temperatures (300–550 K), a VSM magnetometer (Lakeshore) was used in a magnetic field interval of 0 ± 17 kOe. The magnetic domain configuration of the annealed Co_2ZrSn sample was investigated by a magnetic force microscopy (MFM) (Bruker Multimode V Nanoscope 8) equipped with a fully non-magnetic head. An electromagnet is exploited to apply a magnetic field at 600 Oe in the sample plane. MFM images have been acquired via the phase channel in pass 2 in intermittent-contact lift-mode, using CoCr coated MESP-HR tips.

Ab-initio calculations were performed using Vienna Ab Initio Simulation Package (VASP) [49] with projector augmented plane (PAW) method [50], Perdew-Burke-Ernzhof (PBE) functional [51], and Co, Hf_pv, Sn_d potentials [52]. For the calculation of transport properties, the same parameters already described on Ref. [30] were used, while the post-processing was performed in the rigid-band approximation with the BoltZTraP2 code [53]. A 2x2x2 supercell (128 atoms in total) sampled with a 7x7x7 Monkhorst-pack [54] k-point grid was used for both the vacancy simulations and phonon calculations. In the first case, one and two Co atoms were removed from the core of the supercell, bringing the system to a total of 127 and 126 atoms, respectively, thus obtaining $Co_{1.97}ZrSn$ and $Co_{1.94}ZrSn$ stoichiometry, respectively. The same conditions were used for the relaxation calculations of all defective systems in order to obtain the correspondent lattice parameters. The phonon calculations were performed on a pristine supercell. The energy cutoff was always set at 500 eV. The post-processing data treatment for the calculations of phonon and thermal properties were performed in the harmonic approximation with the Phonopy code [55]. The intensity of XRD peaks of Co_2ZrSn was calculated with the PowderCell 2.0 code (PCW) [56].

3. Results and discussion

3.1. Vacancy and Co-site ordering characterization in the Heusler lattice

The Rietveld refinements of synchrotron (Sy.) XRD patterns of the As cast, Annealed, and SPS specimens are shown in Fig. 1. The XRD patterns of the same samples, analysed with a laboratory-scale Cu-Kα diffractometer, are shown in Figure S1 of Supplementary Material. With such instrumentation, powders of Melt-spun and SPS+An. samples were also characterized, as shown in Figure S2 (Supplementary Material). The cell parameters (a) and relative phases abundances in weight percentage are shown in Table 1. In all specimens, the $L2_1$ Heusler was found to be the main phase with small amounts of Co_3Sn_2 and Co_2Zr impurities. Traces of metallic Sn were also found in the As cast and Annealed samples; however, its abundance was small enough to be detectable only using synchrotron light, as well as that of Co_2Zr (always under 2 % wt.).

The amount of vacancy defects present in the Heusler crystal lattice can be quantified using the Rietveld method. As reported by Mahat et al. [57], the intensity of the (200) peak is linked to the atomic order of atoms in the tetrahedral (8c) position, namely Co. Similarly, the (111) reflex is an indicator of octahedral positions ordering (Zr, Sn), while the main peak (220) is independent from the ordering state [58]. Hence, the amount of vacancy defects present in the Heusler crystal lattice can be quantified using the Rietveld method by letting the total Co occupancy free to converge to the refined value. As shown in Fig. 1, two set of Rietveld refinements were performed for each sample. In the pristine model (P), Co occupancy (χ_{Co}) was kept fixed at a value of 1; whereas, in the defective model (V), the presence of vacancy defects was taken into account by letting χ_{Co} free to converge to the refined value. Accordingly, the fit quality of the intensity of the (200) peak is expected to increase as the refinement better describes the occupancy of Co sites. Occupancies of Zr and Sn in the octahedral sites was left fixed at 1 both in P and V models. A schematic depiction of pristine (P) and Co vacancy-defective (V) Heusler crystal structures is shown in Figure S3 of Supplementary Material.

As noticeable from Fig. 1, the Rietveld refinements both in the

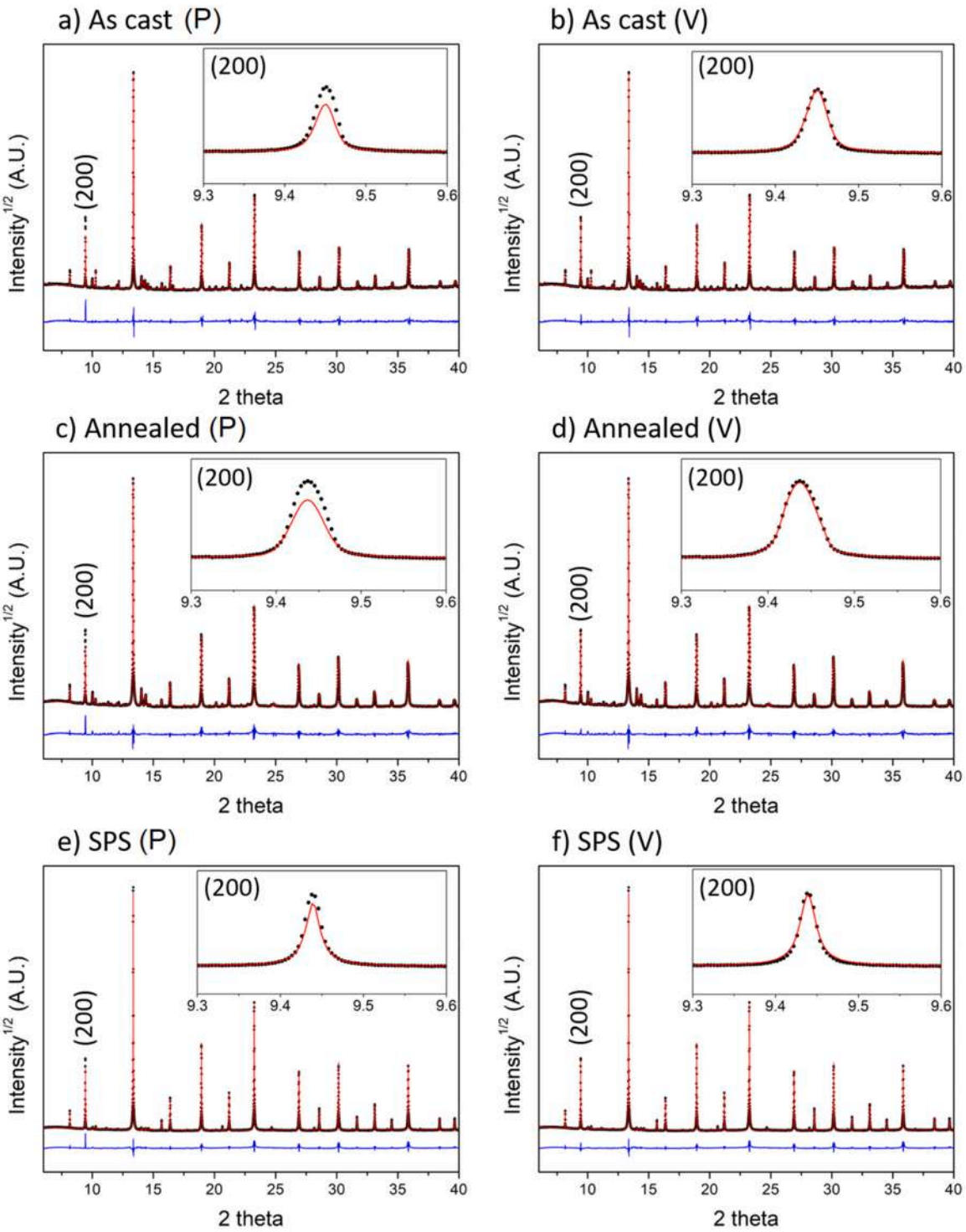

Fig. 1. Rietveld refinements of synchrotron XRD patterns for the as cast (a), annealed (c) and sintered (e) samples, assuming a pristine Heusler structure (P), and for the As cast (b), Annealed (d) and SPS (f) samples, assuming a defective Heusler structure with non-fixed occupancy of the Co-site (V). Insets show a detail of the (200) peak.

pristine and defective conditions well fit the experimental XRD patterns. However, a more careful observation allows to note that, as expected, a rather important discrepancy between the experimental and calculated patterns occurs in correspondence of the peak associated with the (200) plane in the P refinements (insets of Fig. 1).

From a quantitative point of view, three parameters can be considered for determination of the quality of Rietveld refinements: R_{exp}, R_b and χ^2. R_{exp} is a parameter which solely depends on the quality of the XRD measurement, accounting for background noise, signal/noise ratio and linearity of the baseline. The lower R_{exp}, the better is the pattern's quality. As far as R_b is concerned, it quantifies the difference between the calculated fit and the experimental pattern based on the intensity of each point of the diffractogram. The closer R_b is to R_{exp}, the better is the refinement. χ^2, often called the "goodness of fit" parameter, is a composite value which takes into account the least square difference between the calculated and experimental profiles. During the refinement

Table 1
Lattice parameter (a), Co-site occupancy (χ_{Co}), abundance of the Co_3Sn_2 secondary phase (wt%), 200/220 peak intensity ratios for the Co_2ZrSn specimens obtained by different processing routes.

Synchrotron			
	As cast	Annealed	SPS
a (Å)	6.2306	6.2482	6.3085
χ_{Co}	0.84	0.88	0.94
% wt. Co_3Sn_2	5.0	4.1	0.7
% wt. Co_2Zr	1.9	0.8	0.2
% wt. Sn	0.5	0.2	-
I(200)/I(220)%	16.84	15.35	11.40

Cu-Kα					
	As cast	Annealed	SPS + An.	SPS	Melt spun
a (Å)	6.2225	6.2448	6.2677	6.3028	6.3087
χ_{Co}	0.82	0.88	0.91	0.94	0.96
% wt. Co_3Sn_2	4.3	3.7	< 2.0	< 2.0	3.9
I(200)/I(220)%	25.54	19.38	17.74	15.04	14.82

process, χ^2 starts out large when the fit is poor and decreases as the refinement produces better agreement with the data. The closer χ^2 is to 1, the better is considered the model; however, it should be noted that this should never drop below such value. A comprehensive review of the convergence parameters and accuracy figures of merit in Rietveld analysis was provided in 2006 in a seminal work by B.H. Toby [59].

In Table 2 the R_{exp}, R_b, and χ^2 factors are reported for both the P and V sets of refinements. The resulting R_{exp} values are small, indicating that XRD patterns are of good quality. As expected, synchrotron patterns are characterized by R_{exp} values way smaller than those from laboratory-scale Cu-Kα instrument, reflecting the higher accuracy of synchrotron measurements. Smaller values of R_b, and χ^2 were obtained for all samples with the V model, indicating a real occupancy of Co-sites which is lower than 1, and implying that experimental specimens are better described when the presence of Co vacancies is taken into account. The difference of χ^2 between the P and V models ($\Delta\chi^2$) was calculated as in Eq. 3; whereas, ΔR_b was calculated simply as the difference between the R_b% of P and V models.

Table 2
R_{exp}, R_b and χ^2 factors of the pristine (P) and defective (V) Rietveld analysis of Co_2ZrSn samples.

Pristine (P) Synchrotron			
Parameter	As cast	Annealed	SPS
R_{exp} %	0.4060	0.8060	0.8061
R_b %	1.0156	1.4949	1.3793
χ^2	1.7443	1.6525	1.1193

Defective (V) Synchrotron			
Parameter	As cast	Annealed	SPS
R_{exp} %	0.4060	0.8060	0.8061
R_b %	0.7592	1.3148	1.2951
χ^2	1.4350	1.4897	1.1098
ΔR_b	0.2564	0.1801	0.0842
$\Delta\chi^2$ (%)	16.70	9.85	0.85

Pristine (P) Cu-Kα					
Parameter	As cast	Annealed	SPS + An.	SPS	Melt spun
R_{exp} %	1.6625	1.3718	1.4068	1.4688	1.4092
R_b %	2.6493	1.8876	2.515	2.5885	1.9589
χ^2	1.6580	1.9106	2.4103	2.4007	1.6377

Defective (V) Cu-Kα					
Parameter	As cast	Annealed	SPS + An.	SPS	Melt spun
R_{exp} %	1.6625	1.3718	1.4068	1.4688	1.4092
R_b %	2.4385	1.7388	2.3811	2.4586	1.8633
χ^2	1.4177	1.7036	2.2014	2.3656	1.6273
ΔR_b	0.2108	0.1488	0.1339	0.1299	0.0956
$\Delta\chi^2$ (%)	14.49	10.83	8.67	1.46	0.64

$$\Delta\chi^2 = \frac{\chi_P^2 - \chi_V^2}{\chi_P^2} \cdot 100 \quad (3)$$

Considering the results obtained with the V model, the most defective sample of the series was observed to be the arc-melted specimen (As cast), which presented from synchrotron data the lowest Co site occupancy of 0.84, leading to a nominal $Co_{1.68}ZrSn$ formula unit. A similar occupancy of 0.82 was found from the refinement of the laboratory-scale pattern, leading to a $Co_{1.64}ZrSn$ formula unit, in strong agreement with that obtained from synchrotron. The same sample after annealing (Annealed) was found with an increased occupancy of Co sites, equal to 0.88 both from synchrotron and Cu-Kα radiation, bringing the formula unit to $Co_{1.76}ZrSn$. On the other hand, the alloy synthesized by rapid solidification (Melt-spun) was observed to be the closest to the pristine stoichiometry, having χ_{Co} of 0.96 and a $Co_{1.92}ZrSn$ stoichiometry. This is because the rapid cooling allows to expand the solubility limit of Co inside the Heusler compound, allowing to force the stoichiometry towards a Co-richer composition. As the rapidly solidified powder is subjected to the heat treatment involved in the spark plasma sintering process, a shift towards more stable conditions begins, resulting in a slight decrease of χ_{Co} to a value of 0.94 ($Co_{1.88}ZrSn$) for the SPS specimen. When the so obtained SPS sample was subsequently annealed for an extensive period (SPS+An.), Co occupancy kept decreasing as the Heusler compound composition shifts towards the thermodynamically stable stoichiometry, leading to a χ_{Co} of 0.91 ($Co_{1.82}ZrSn$), which is extremely close to what observed for the Annealed sample. On the other hand, considering the P case, no difference in Co occupancy was estimated, as this model, by definition, does not take into account deviations from the pristine stoichiometry.

The trend of $\Delta\chi^2$ and ΔR_b as a function of χ_{Co} are shown in Figs. 2(a) and 2(b). Interestingly, the values of $\Delta\chi^2$ and ΔR_b increase with the increasing concentration of vacancies inside the specimens. This is to be expected, as for samples having stoichiometry close to the pristine (i.e. Melt-spun and SPS), V and P models are similar. Coherently, as the samples become more defective (or, as χ_{Co} become increasingly lower than 1), P begins to fit the experimental data less effectively, thus increasing $\Delta\chi^2$ and ΔR_b. In fact, $\Delta\chi^2$ was calculated being 0.64 % and 1.46 % (Cu-Kα), respectively, for the melt-spun and SPS specimens, which are the least defective specimens. The more defective SPS+An. and Annealed samples show higher $\Delta\chi^2$ around 9–11 % (Cu-Kα). The most defective sample, the As cast, presents the highest $\Delta\chi^2$ of 14.49 % (Cu-Kα) and 16.70 % (synchrotron), indicating that the V model is considerably better in describing such specimen. From Fig. 2(a) and Fig. 2(b) it is also possible to note how the increase in goodness of fit is rather linear with the increasing χ_{Co}, ideally reaching a $\Delta\chi^2$ equal to zero when χ_{Co} approaches 1. This would happen for an ideal pristine sample, for which the P and V models would coincide. Analogous considerations are applicable for ΔR_b, which shows a linear trend as well as a function of χ_{Co}.

Anti-site defects are also known to be common in Heusler alloys [45]. In order to exclude that such effect could be caused also by Zr or Sn anti-site defects in 8c, two additional Rietveld refinements were performed, as an example, for the As cast sample, imposing Zr and Sn anti-sites as the only defect present in the system. An arbitrary 0.33 occupancy factor in the 8c site was assigned to Zr and Sn as initial conditions. Such two models, which will be labelled as A-Zr and A-Sn, respectively, were first computed in their fixed initial conditions. Then, the Zr and Sn occupancies were unlocked and the models let free to converge towards the optimal values. As highlighted in Figure S4 of Supplementary Material, the introduction of elements with atomic number higher than 27 in the 8c site have the effect of decreasing the intensity of the (200) peak. Indeed, as noticeable from Figure S5 of Supplementary Material, the quality of fit on the (200) peak dramatically decreases with respect to P. Unsurprisingly, as soon as Zr and Sn occupancies are let free to converge, the refinement rapidly brings such

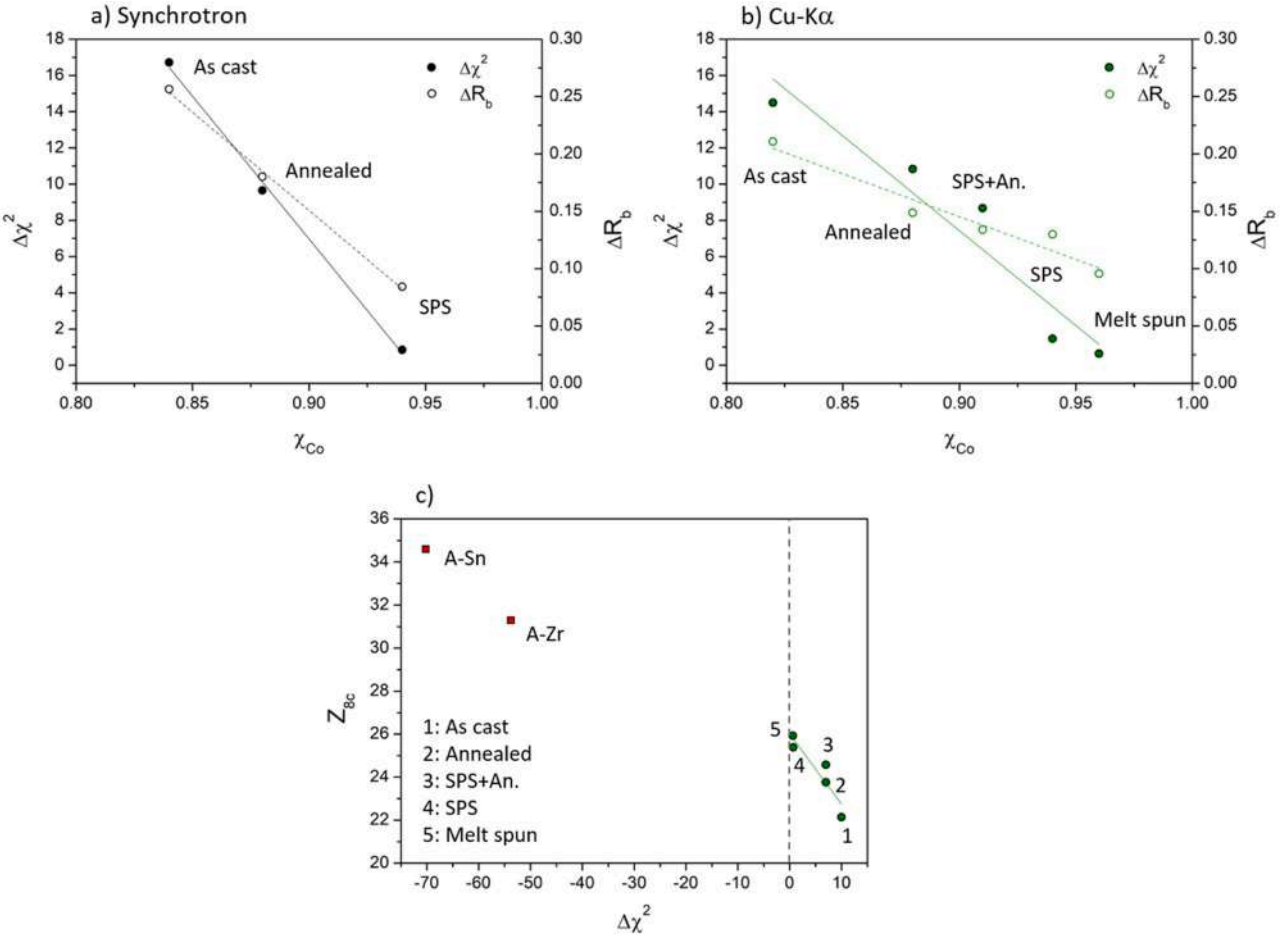

Fig. 2. (a) $\Delta\chi^2$ as a function of χ_{Co} of the refinements from synchrotron patterns; (b) $\Delta\chi^2$ as a function of χ_{Co} of the refinements from laboratory-scale Cu-Kα patterns; (c) Z_{8c} as a function of $\Delta\chi^2$ of all Rietveld refinements from laboratory-scale measurements.

values at zero, ultimately returning outcomes which are analogous to P. At this point, if the total Co occupancy is unlocked as well, the refinements become as the V model. Considering the A-Zr and A-Sn models, when compared with As-cast P, $\Delta\chi^2$ values of −54 % and −70 % are obtained. The negative sign is indicative of the fact that in these cases, the defective model is less reliable than the non-defective, as the fit on the intensity and profile of the (200) peak is worsened after that anti-site defects are introduced in the calculation. $\Delta\chi^2$ of A-Zr and A-Sn was calculated as follows:

$$\Delta\chi^2 = \frac{\chi_P^2 - \chi_{A-Zr/Sn}^2}{\chi_P^2} \cdot 100 \quad (4)$$

This is shown in Fig. 2(c), where the average atomic number in the 8c site (Z_{8c}) was plotted as a function of $\Delta\chi^2$. Here, it is possible to note that,

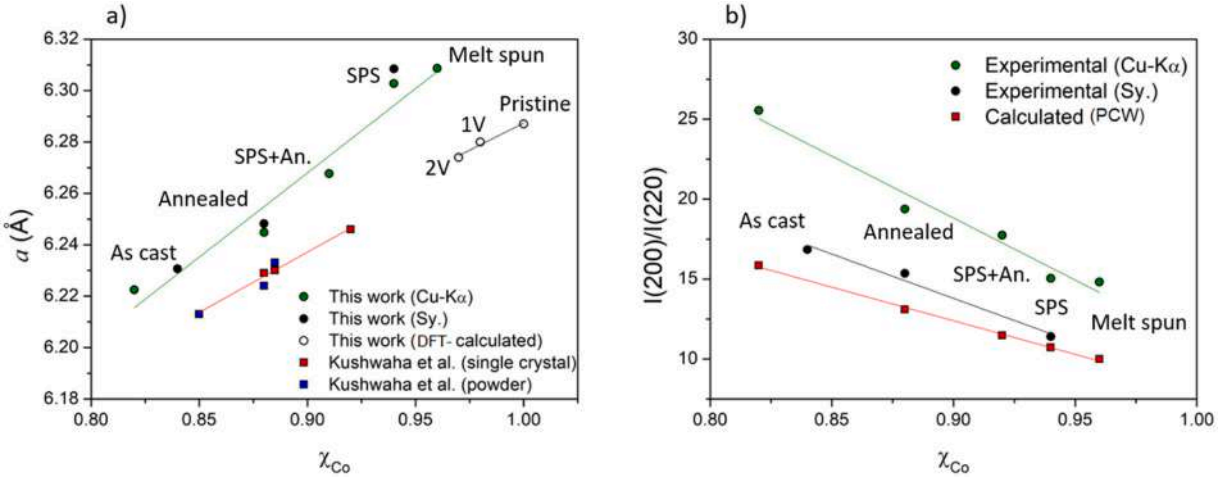

Fig. 3. Lattice parameter (a) and I(200)/I(220) (b) as a function of χ_{Co} for the various Co_2ZrSn samples. PCW calculated I(200)/I(220) values for an ideal Co_2ZrSn crystal are also reported. Data of Kushwaha et al. are from Ref. [43]. DFT calculated data will be discussed in 3.5.

again, $\Delta\chi^2$ tends to be almost zero for an average atomic number in 8c of 27, which would be satisfied for a pristine sample. Considering the V model, $\Delta\chi^2$ becomes increasingly positive for samples with stoichiometry further from the ideal Co_2ZrSn, meaning that the V model progressively better describes highly defective specimens (see Eq. 3). On the other hand, $\Delta\chi^2$ of A-Zr and A-Sn are negative (Eq. 4), meaning that such models are worse than P in fitting the experimental values. Additionally, their absolute $\Delta\chi^2$ values of 53 % (A-Zr) and 70 % (A-Sn) are far from being acceptable to describe our set of samples.

In Fig. 3(a), the lattice parameters of Co_2ZrSn specimens are plotted as a function of the Co occupancy (χ_{Co}). The values from synchrotron and laboratory-scale data are in in strong agreement. Considering Fig. 3 (a), the first aspect to notice is that a scales linearly with χ_{Co} similarly to what already found by Kushwaha et al. [43], who obtained extremely comparable results in a previous study. The linear shrinking of the a with the decreasing χ_{Co} is compatible with the progressive increasing of the vacancy concentration, as also previously reported for single crystal samples [43]. Such trend is impossible to explain considering other types of defects, as intrinsic anti-sites with Zr and Sn always involve atoms with an atomic radius larger than Co, leading to a lattice expansion. Such statement was confirmed by ab-initio calculations performed on several defective Co_2ZrSn systems, which will be presented more in detail in 3.5.

The disorder in the 8c site was also evaluated for the various samples without the use of the Rietveld refinement method by measuring the experimental intensity ratios of (200) and (220) peaks, or I(200)/I(220) (see Table 1). In Fig. 3(b), the trend of I(200)/I(220) are reported as a function of χ_{Co}, showing a decreasing linear trend which is coherent to what expected from the theory (calculated with the Powder Diffraction Cell, PCW, code). In fact, as highlighted in Figure S4 in Supplementary Material, I(200)/I(220) decrease with the increasing vacancy concentration in 8c, coherently to what found experimentally. Such decreasing trend is incompatible with those obtained by simulating the effect of Zr or Sn anti-site defects (PCW), as shown in Figure S4 as well. Indeed, since both Zr and Sn have higher atomic number than Co, the presence of such anti-sites in the 8c position would lead to a decrease of the I(200)/I (220) ratio with respect to the pristine compound, which is incompatible with experimental observations. Being synchrotron measurements more accurate in evaluating the intensity of XRD peaks, experimental values from synchrotron are extremely close to those calculated from the theory, while the trend extracted from Cu-Kα patterns is slightly more distant. By extrapolating at $\chi_{Co}= 1$ the trend obtained by synchrotron data, a I(200)/I(220) of 8.25 is observed, which is extremely close to the 8.67 predicted for a perfect Co_2ZrSn crystal (PCW). The extrapolated I (200)/I(220) at $\chi_{Co}= 1$ of the Cu-Kα trend is 11.06. Overall, the experimental and simulated I(200)/I(220) trends as a function of χ_{Co} are in good agreement, especially considering synchrotron data, leading to the same conclusions deduced from Rietveld refinements, and indicating vacancies as the main defect affecting the sites of Co.

As noticeable from Table 1, having the SPS and melt spun alloys approximately the same Co occupancy, they present accordingly very similar I(200)/I(220) values. Being the heat-treated samples the closest to thermodynamic conditions, it is possible to state that the presence of vacancies or, more in general, Co-site disorder is thermodynamically favoured, as also showed by DFT calculations (see Section 2.5). This can be better understood considering the processing route of the SPS specimen. During the melt-spinning process, cooling rates between 10^4 and 10^5 K/s are reached, allowing to obtain alloys in metastable conditions [60]. The Melt-spun material was found to be the least defective, presenting a χ_{Co} of 0.96 and thus the largest lattice parameter. This is because the rapid cooling allows to expand the solubility limit of Co inside the Heusler compound, allowing to force the stoichiometry towards a Co-richer composition. As the rapidly solidified powder is subjected to the heat treatment involved in the spark plasma sintering process, a shift towards more stable conditions begins, resulting in a slight decrease of χ_{Co} and thus a. Being the difference of χ_{Co} small, extremely similar values of I(200)/I(220) ratio are measured for such two specimens. When the so obtained SPS sample was subsequently annealed for an extensive period (SPS+An. specimen), the Co occupancy kept decreasing as the Heusler compound composition shifts towards the thermodynamically favourite stoichiometry. The usual associated shrinking of lattice parameter is again reported. Here, a noticeable reduction of the I(200)/I(220) ratio is also observed. Similarly, the arc melted as cast sample, which was subjected to a typical cooling rate between 10 and 10^2 K/s, is located on the edge of a and χ_{Co} values range.

3.2. Microstructural and texture properties

In Fig. 4, electron backscattered SEM images of the As cast, Annealed and SPS samples are presented. Having the specimens been polished down to a 40 nm mesh, Heusler phase grains with different orientations appear with different gray levels due to backscattered electron diffraction. Additionally, the secondary Co_3Sn_2 is easily recognizable, and it is mainly located at the grain boundaries of the Heusler phase. In the case of the SPS sample, the amount of the secondary phase is significantly lower than in the As cast and Annealed samples, in agreement with the results of the Rietveld refinement of the XRD patterns reported in Table 1.

EDS spectra revealed an average atomic compositions equal to 49 % Co, 24 % Zr, 26 % Sn for all samples (considering an intrinsic error of the EDS technique approximately of 1 % for each element). Spot analysis showed a composition of the secondary phase approximately of 61 % Co, 4 % Zr, 35 % Sn, confirming the presence of an intermetallic Co_3Sn_2 compound, as suggested by XRD patterns (see Fig. 1). The stoichiometry of such phase is approximately the same in all specimens with amounts of Zr fluctuating between 3 % and 4 %. Due to its low amount, the Co_2Zr secondary phase was not detected with the EDS analysis; however, its presence was assessed from synchrotron XRD measurements. The composition of the Heusler phase in the different samples is reported in Table 3. As it can be noticed, compositions measured by EDS satisfactorily match the stoichiometry calculated from the Co-site occupancy values resulting from the Rietveld refinement. Further conclusions solely based on EDS data are difficult to assess, as the intrinsic error relative to the EDS technique in such samples is on the order of 1 %. Nevertheless, two observations can still be made: first, it is noticeable that the average value of Co composition increase as both χ_{Co} and a (see Table 1) increase, as to be expected; second, it is important to note that in the as cast and SPS samples, the standard deviation on the atomic percentages is larger than the technique's intrinsic error, suggesting a slight non-homogeneity of composition in such samples. On the contrary, the atomic percentages in the Heusler phase for the annealed specimens (Annealed and SPS+An.) are less dispersed, suggesting an increase of homogeneity derived from the heat treatment.

Quantitative information on grain size, shape, and preferential orientations can be extracted from the analysis by EBSD technique. Grains size and grains aspect ratio distributions were fitted with Log-normal functions, from which the respective average values were calculated. In Fig. 5(a), Fig. 5(c), and Fig. 5(e), the EBSD grain orientation maps are presented. Here, each grain is colored based on its orientation with respect to a certain considered axis, which is in this case the direction of the cooling gradient for the As cast and Annealed samples, and the direction of the applied pressure during sintering for the SPS specimen. Since grains appeared randomly colored along the whole investigated area, it is possible to conclude that no preferential orientations are present in the samples. Additionally, grains appear qualitatively equiaxial, presenting an average ellipsoid aspect ratio of approximately 1.5 in all the specimens (see Figure S6 of Supplementary Material), indicating rather circularly shaped crystals. From EBSD maps, grain size distributions were calculated and reported in Figs. 5(b), 5(d), and 5(f). Having been subjected to the fastest cooling rate during the rapid solidification process, it is not a surprise that the lowest average grain size is shown by the SPS sample, showing an average value between 2 μm

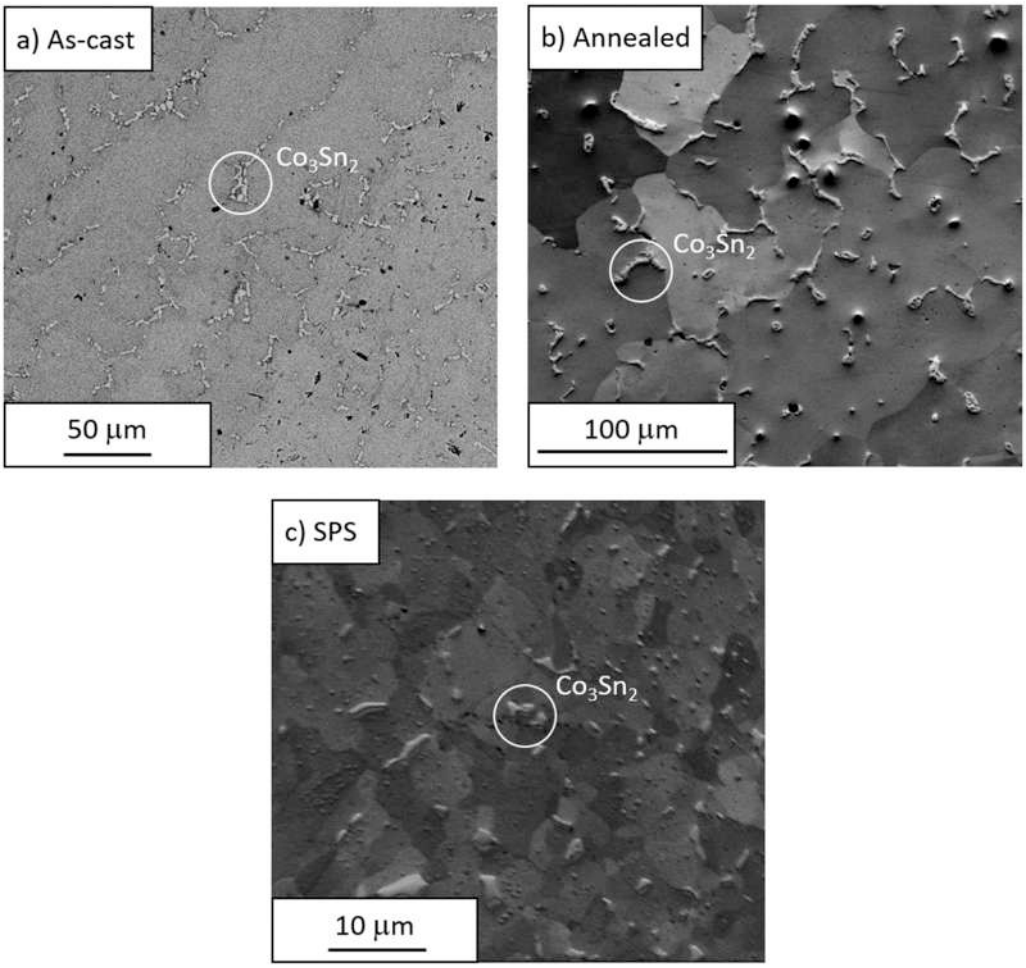

Fig. 4. SEM backscattered images of the as cast (a), annealed (b), and sintered (c) Co_2ZrSn samples.

Table 3
Co-site occupancy (χ_{Co}), phase stoichiometry (calculated from values χ_{Co} obtained from XRD data), and EDS elemental composition of the Heusler phase for the various samples processed by different techniques.

Sample	χ_{Co}	Phase Stoichiometry (XRD)	EDS elemental composition (at%)		
			Co	Zr	Sn
As cast (Sy.)	0.84	$Co_{1.68}ZrSn$	46.5 ± 2.0	26.5 ± 2.0	28.0 ± 2.0
As cast (Cu-Kα)	0.82	$Co_{1.64}ZrSn$			
Annealed	0.88	$Co_{1.76}ZrSn$	47.0 ± 1.0	26.0 ± 1.0	27.0 ± 1.0
SPS	0.94	$Co_{1.88}ZrSn$	48.0 ± 1.5	25.5 ± 1.5	26.5 ± 1.5
SPS + An.	0.91	$Co_{1.82}ZrSn$	48.0 ± 1.0	26.0 ± 1.0	26.0 ± 1.0
Melt spun	0.96	$Co_{1.92}ZrSn$	49.0 ± 1.5	25.0 ± 1.5	26.0 ± 1.5

and 3 µm. Being the cooling rate during the arc-melting lower than that in melt-spinning, the As cast sample present considerably larger grains with an average diameter of about 55 µm. This value was not found to change after the annealing treatment.

3.3. Transport properties

In Fig. 6(a) and Fig. 6(b), the results of the Hall effect measurements for the Annealed specimen are shown as an example (see Figure S7 of Supplementary Material for those of the As cast and SPS specimens). As typical of ferromagnetic materials, the Hall effect consists of ordinary Hall effect (OHE), which is proportional to the applied magnetic field, and anomalous Hall effect (AHE), which depends on the spontaneous magnetization. Above + 1 T and below −1 T, the measured resistance scales linearly with the magnetic field, as in Fig. 6(b). As the resistance was found to have approximately the same slope as a function of the field at various temperatures, rather constant Hall coefficients (R_H) were obtained, as shown in Fig. 6(c).

Fig. 7 shows the temperature dependence of the electronic transport properties for As cast, Annealed, and SPS samples. The Seebeck coefficient was measured between 300 and 800 K, empty symbols in Fig. 8(a), showing a similar behaviour for all samples. As previously reported in Ref. [34], the value of the Seebeck coefficient is negative and $|S|$ shows a linear increase from room temperature to approximately T_C, followed by a plateau at higher temperatures. The absolute values of S for the different measured samples are directly proportional to the Co-site occupancy|. The measurements below 300 K, filled symbols in Fig. 7(a), also show negative values of S down to 173 K, confirming that the electrons are the main charge carriers in the whole temperature range explored.

The sign of the slope in the Hall resistance measurements is usually associated to the sign of the majority charge carriers. The positive slopes observed in the measurements between and 270 K, Fig. 6(b), would indicate the prevalence of holes as majoritarian charge carriers, in contradiction with the results of the Seebeck coefficient measurements. It is possible to explain this apparent contradiction assuming a multiple-bands effect, that we will confirmed by the complex band structure calculated by DFT (3.5). According to a simple two band model, the

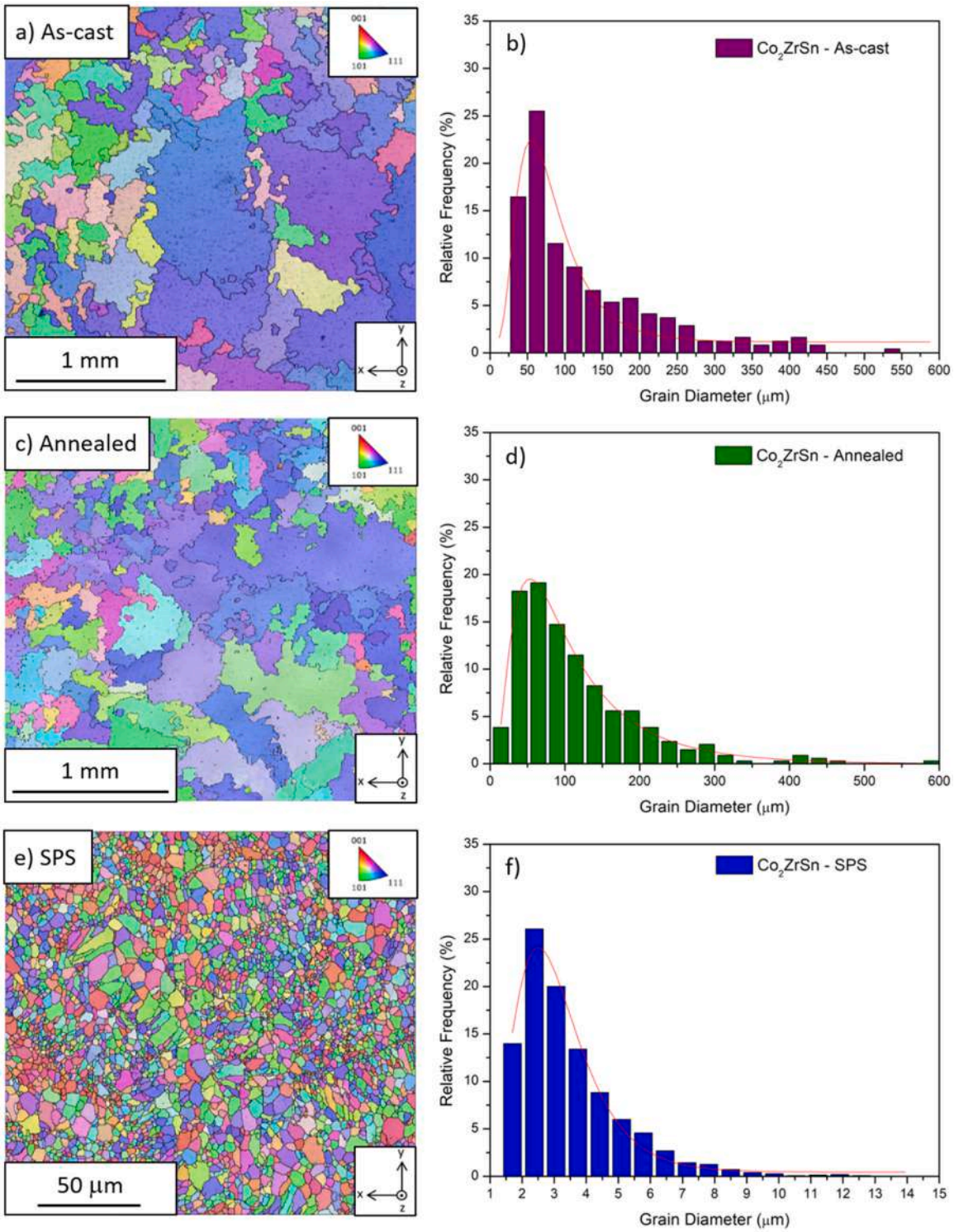

Fig. 5. EBSD grain orientation maps (along the z direction) of the As cast (a), Annealed (c) and SPS (e) samples. Grain size distributions of the As cast (b), Annealed (d) and SPS (f) samples. The red line is the fitted Log-normal distribution.

Seebeck coefficient and the Hall resistance can be expressed by Eqs. 5 and 6 [44]:

$$S = \frac{S_p \upsilon_p p - S_n \nu_n n}{p\upsilon_p + n\upsilon_n} \tag{5}$$

$$R_H = \frac{1}{e} \frac{p\upsilon_p^2 - n\upsilon_n^2}{\left(p\upsilon_p + n\upsilon_n\right)^2} \tag{6}$$

where, $S_{n/p}$ is the contribution to the Seebeck coefficient determined by electrons/holes, $\nu_{n/p}$ the mobility of electrons/holes, and n and p the concentrations of electrons and holes, respectively. In such framework, minority but mobile charge carriers (holes) dominate the Hall coefficient (Eq. 6), whereas majoritarian but less mobile electrons dominate in the Seebeck coefficient (Eq. 5). This is compatible with the band structure of pristine and defective Co_2ZrSn, as presented in 3.5 (see Figs. 10 and 11).

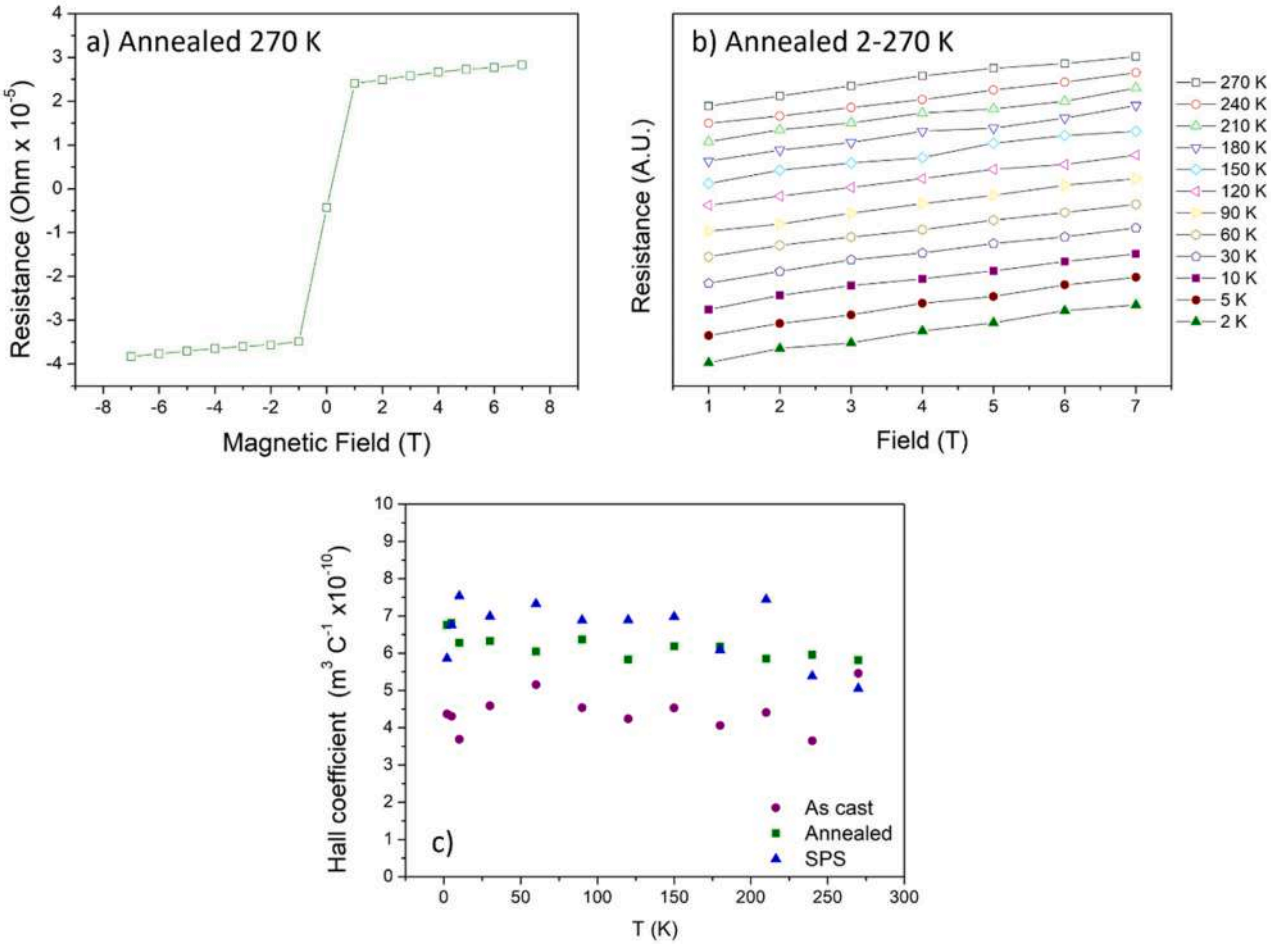

Fig. 6. Hall resistance for the annealed sample measured at 270 K (a). Hall resistance as a function of the applied magnetic field measured in the temperature range between 3 and 270 K for the annealed sample (b). Hall coefficient, R_H, between 3 and 270 K (c) for the annealed sample.

Concerning the electrical conductivity, Fig. 7(b), it decreases almost linearly from room temperature to a minimum value and subsequently weakly rises. For this type of compounds, the temperature at which σ changes its slope corresponds to the Curie point, T_C [28]. Here, the Annealed sample shows a slightly different value of T_C with respect to the as-prepared ones (As cast and SPS), probably due to the observed composition fluctuations of the Heusler phase in the different samples, as reported in 3.2. In fact, as already reported in Ref. [30,43], even small compositional inhomogeneity can have an effect on T_C, leading to the remarkable scattering of data observed in literature [29,36–42]. Above the Curie point, the values of electrical conductivity scales with Co-site occupancy, showing the lowest values for the most defective sample (i.e. As cast).

Due to the square dependence on S, the power factor ($PF = S^2\sigma$) shows a trend similar to the one of the Seebeck coefficient, consisting on a rather linear increase until T_C followed by a plateau, as shown in Fig. 7 (c). At 773 K, values of 0.296 mW m^{-1} K^{-2}, 0.338 mW m^{-1} K^{-2}, and 0.400 mW m^{-1} K^{-2} were obtained for the As cast, Annealed and SPS samples, respectively. These values scale with the Co-site occupancy, indicating that the overall electronic transport properties are strongly influenced by the vacancy concentration.

Fig. 7(d) shows the electrical resistivity, R, as a function of temperature between 2 K and 300 K. A change of the dependency of R on T was found around 50–70 K for all the samples. At lower temperatures, the dependence is parabolic (solid line), while, increasing the temperature, R becomes proportional to T^x (dashed line). In particular, the As cast, Annealed and SPS samples show a regime change from parabolic to T^x (with x equal to 1.40, 1.57 and 1.41, respectively) at 47 K, 64 K and 69 K, respectively. For weak ferromagnets, the dependency of the electrical resistivity on T was modelled in 1975 by Ueda and Moriya [61]. Later, such model was used by Hordequin et al. [62] to describe the low-T R/T dependency of the half-metallic NiMnSb Heusler alloy. The same considerations were also applied in other studies to rationalize the electron scattering mechanisms of NiMnSb and other half-metallic compounds [35,63]. According to Ueda and Moriya, electron-magnon (spin-wave) scattering results in specific contributions to the overall electrical resistance characterized by different coefficients [61] according to the electron-magnon scattering mechanism involved (either longitudinal [non-spin-flip] or transverse [spin-flip]), and varying in every case as T^2 at low temperatures ($T << T_C$) and as $T^{5/3}$ when T approaches T_C. Therefore, a T^2 dependency of the electrical resistance is expected in Co_2ZrSn at temperatures sufficiently lower than T_C.

As far as electron-phonon scattering is concerned, the Bloch-Grüneisen model shows that at low temperature, electrical resistivity does not depend on phonon-induced scattering, as their frequency is too small to significantly perturb the electron density. Approaching the Bloch-Grüneisen limit, phonon frequency becomes sufficiently high to cause an increase of electrical resistivity, which is modelled to scale linearly with T [64].

In the half-metallic ferromagnetic NiMnSb, the measurement of electrical resistivity was found to give extremely similar results as those found in this work for Co_2ZrSn. These were interpreted as evidence of the presence of an actual band gap on the minority spin sub-band, using a combination of the Ueda-Moriya and Bloch-Grüneisen models. In NiMnSb, a crossover temperature (T^*) was reported by several studies around 80–100 K. Above such limit, the resistivity was found to scale

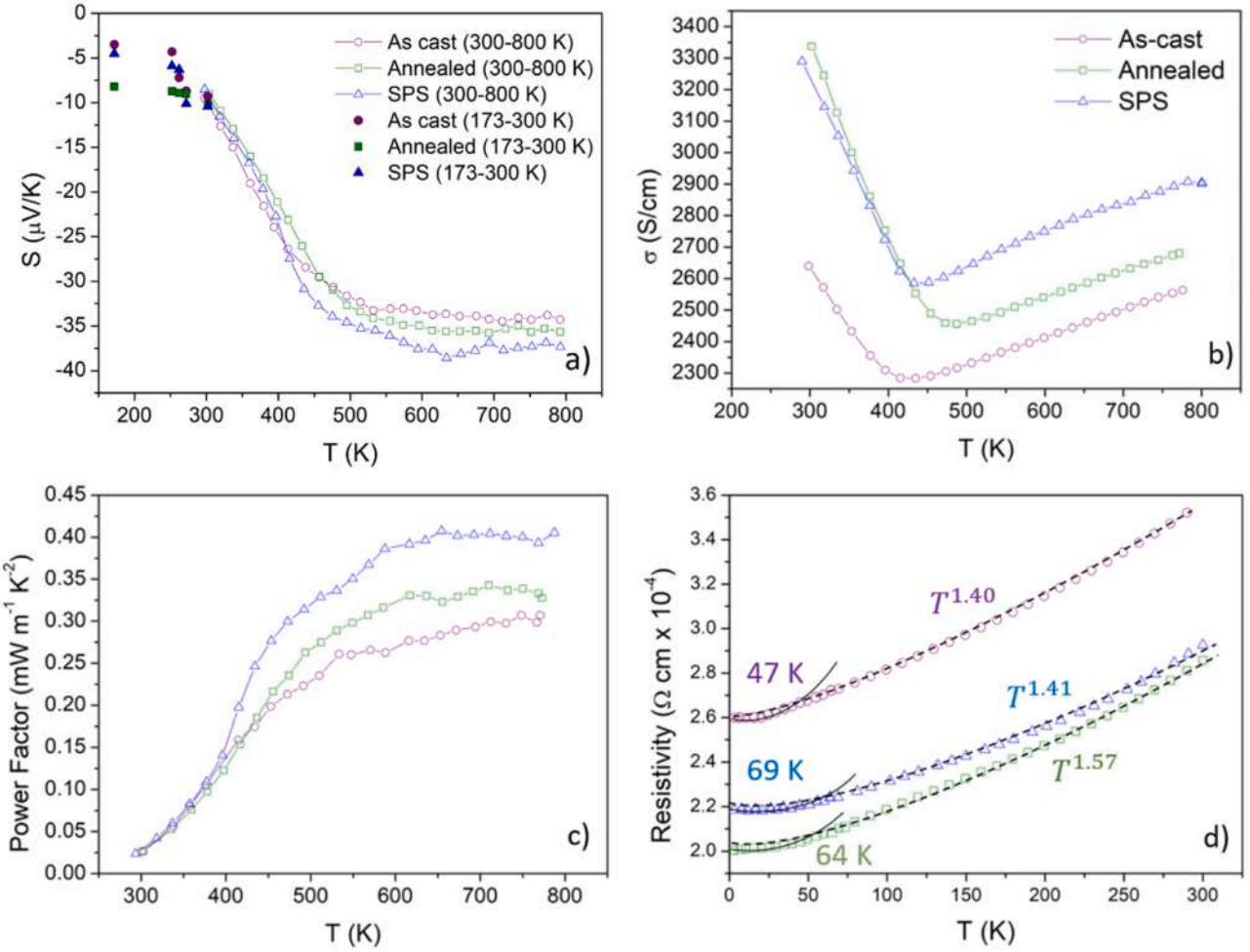

Fig. 7. Seebeck coefficient (empty and full symbols respectively indicate measurements above and below 300 K) (a), electrical conductivity (b) and power factor (c) measured as a function of temperature. Electrical resistivity measured between 2 K and 300 K (d).

with T^x ($x = 1.35$–1.55, depending on the study [35,62]). In such temperature range, phonon-related resistivity gives a linear contribution with T, as prescribed by the Bloch-Grüneisen model. Also, spin diffusion was accounted with a $T^{5/3}$ contribution, as predicted by Ueda and Moriya (Eq. 6). Spin waves would also contribute with a linear T term [61]. Thus, the total exponent on temperature should be a combination of those of the various contributions, being comprised between 1 and 5/3. Accordingly, experimental exponents between 1.35 and 1.55 were observed [35,62]. Below T^*, resistivity was measured to decrease slower, as the trend was experimentally found to be proportional to T^2. This coincides with an electron scattering essentially caused predominantly by spin waves, as demonstrated by Ueda and Moriya [61]. As at such temperatures the phonon contribution is negligible (according to the Bloch-Grüneisen model), the trend of resistivity was reported to be ultimately caused by magnon-induced scattering.

As a matter of fact, in some Heusler alloys behaving as half metallic ferromagnets [62,65,66] the experimental resistance at low temperatures (where the phonon contribution is negligible) is best described by multiplying the T^2 law by an exponential factor of the type $\exp(-E_g/k_BT)$. The exponential suppression of the magnon term represents the effect of the energy gap E_g for the minority spin electronic states at the Fermi level, which effectively inhibits electron-magnon scattering involving spin flip [63]. However, the exponential suppression is typically observed [62,63,65,66] below a characteristic crossover temperature $T^* \approx E_g/k_B$. In the present case, the band gap for the Co_2ZrSn compound is definitely larger than the values usually observed in Heusler alloys characterized by an exponential suppression of the T^2 term, such as Co_2MnGe [66] and Co_2FeSi [65] (E_g being around 0.35 eV for Co_2ZrSn (see 3.5 and [30]) whereas it is less than 10 meV in Co_2MnGe and Co_2FeSi [65,66]). As a consequence, the condition $k_BT << E_g$ is always fulfilled in Co_2ZrSn (the crossover temperature being above 4000 K), so that spin-flip scattering processes are suppressed in the whole interval of investigated temperatures ($4\ K \leq T \leq 300\ K$). The observed T^2 dependency is ensured by non-spin-flip electron-magnon scattering, as theoretically predicted for weak itinerant ferromagnets [61] and experimentally observed in NiMnSb [62].

Overall, it is worth noting that the resistivity trend shown in Fig. 7(d) for Co_2ZrSn is the same measured for the half-metallic NiMnSb Heusler alloy [35,62]. Although this evidence alone is not deemed sufficient to experimentally prove the presence of a half-metallic band-gap in Co_2ZrSn, such behavior is not incompatible with the presence of such gap at low temperatures. The same crossover at low-T was found also in the trend of magnetization (M) on temperature of Co_2ZrSn (see 3.4), similarly again to what measured for NiMnSb [35,62,67,68]. This was again linked to the presence of the same half-metallic state below a certain T. For Co_2ZrSn, the previously obtained crossover temperature by the measurement of M vs. T was around 70 K [30], which is consistent with the values found in this work both from the characterization of electrical conductivities, Fig. 7(d), and of that of magnetic properties (see 3.4).

Considering both the low and high T profile of the electrical conductivity, several observations can be made. Comparing the as cast and annealed samples, the latter shows significantly larger values than the former over the entire range of temperatures. Being these two specimens

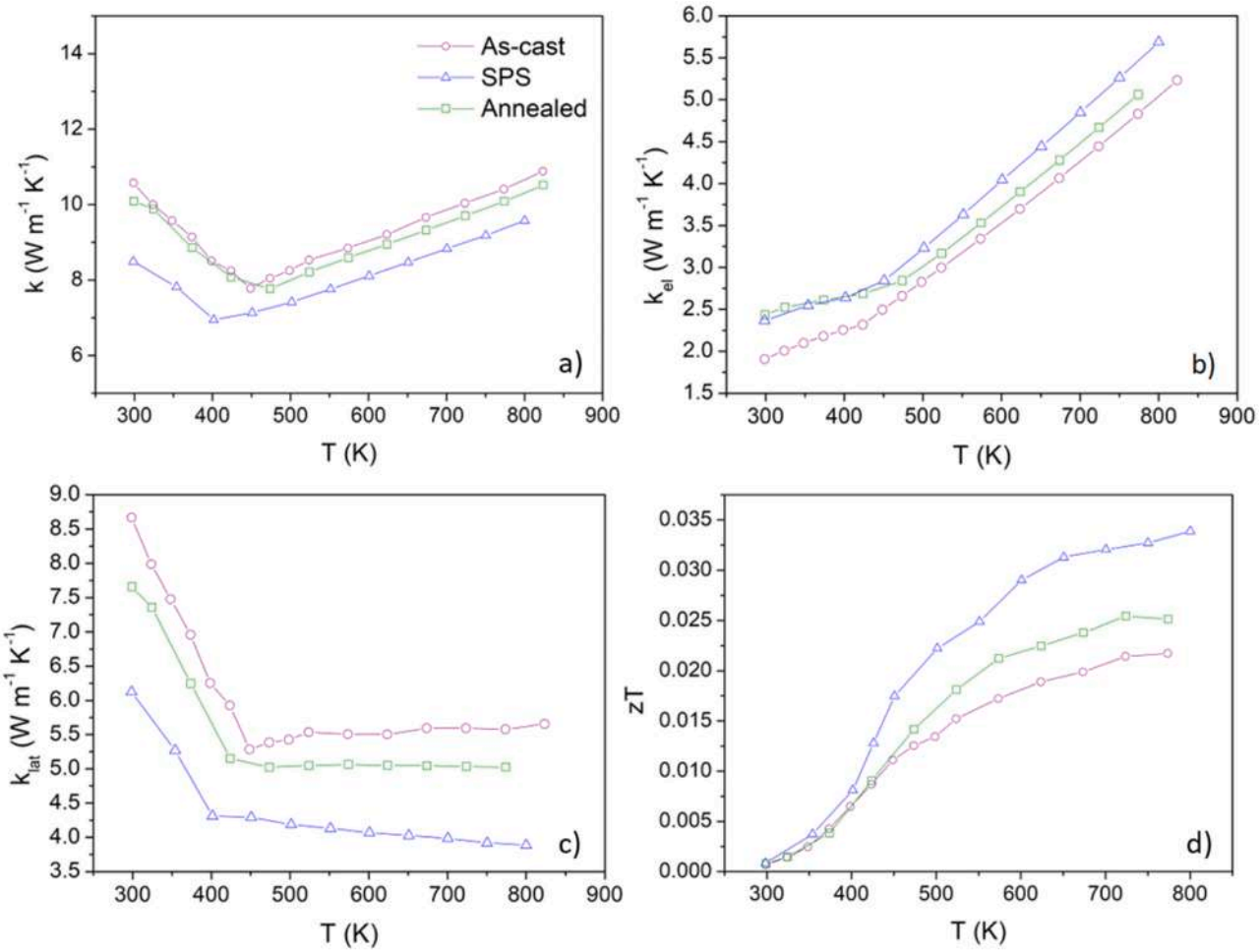

Fig. 8. Thermal conductivity, k, (a), electronic contribution to thermal conductivity, k_{el} (b), lattice contribution to thermal conductivity, k_{lat} (c), thermoelectric figure of merit zT (d) of As cast, Annealed and SPS samples.

microstructurally very similar (Fig. 5), the difference of σ can be linked to compositional effects, showing that the increase of Co-site occupancy has a beneficial effect on electrical conductivity. When the Annealed and SPS samples are taken into account, their electrical conductivities are very similar between room temperature and 450 K, while at higher temperature the SPS sample shows larger values than the Annealed. Conversely, between 2 K and 300 K, σ of the Annealed sample becomes larger with respect to the that of SPS. According to the different χ_{Co} values in the two samples, the electrical conductivity of the SPS specimen ($\chi_{Co} = 0.94$) is expected to be significantly larger than the Annealed ($\chi_{Co} = 0.88$) over the whole temperature range. However, the microstructures of the two specimens, Fig. 5, show a larger grain boundary density for the SPS sample with respect to the Annealed. Since the charge carrier scattering due to grain boundaries is dominant at lower temperature [69], the larger values of σ observed for the Annealed sample between 2 K and 300 K can be explained in terms of lower grain boundary density. At higher temperature, where the grain-boundary contribution to the carrier scattering is limited, the larger values found for the SPS specimen can be interpreted in terms of lower vacancy concentration (i.e. larger χ_{Co}). This interpretation is in agreement with the fact that the electronic properties of Co_2ZrSn almost exclusively depend on Co atoms as a direct consequence of its density of states at the Fermi level [30].

From thermal diffusivity values (Figure S8 in the Supplementary Material), the thermal conductivity, *k*, was obtained, Fig. 8(a), by multiplying them by the respective sample densities (8.22 g cm^{-3} for the As cast and Annealed, 7.89 g cm^{-3} for the SPS) and the Co_2ZrSn phase specific heat capacity, C_P, (see Figure S9 of Supplementary Material). The trends of *k* as a function of *T* are quite similar to those of σ, as a linear decrease from room temperature to T_C is followed by a linear increase above the Curie point. This trend is analogous to that reported for the similar Co_2HfSn Heusler alloy [32]. The electronic contribution to the thermal conductivity, k_{el}, was calculated using the Wiedemann-Franz law ($k_{el} = L\sigma T$, with $L = 1.5 + \exp\left[-\frac{|S|}{116}\right]$ $W\Omega K^{-2}$ as proposed by Snyder et al. [70]), and it is reported in Fig. 8(b). The lattice contribution, k_{lat}, was estimated as $k_{lat} = k - k_{el}$ and is reported in Fig. 8 (c). Since Annealed and SPS samples have comparable values of σ, the corresponding k_{el} were found to be similar as well; whereas, the As cast sample, which exhibits the lowest σ values, shows the lowest k_{el} contribution, accordingly. As far as k_{lat} is concerned, the as cast and annealed specimens present close values while the SPS sample has the lowest k_{lat}, Fig. 8(c). In the case of the SPS sample, the lowest values of k can be interpreted in terms of a finer microstructure (Fig. 5) and lower density with respect to the As cast and Annealed samples. However, the decrease in density is only about 4 % while the decrease of *k* and k_{lat} at 300 K are about 20 % and 30 %, respectively, suggesting a significant effect of the larger grain boundary density on phonon scattering. Such effect was successfully studied using a novel modelling approach, constituting an innovative framework for the analysis of thermal transport in defective polycrystalline materials by Sood et al. [71]. It has to be reminded that, below T_C, magnons also significantly contribute to k_{lat}, as it will be explained more in detail in 3.5.

The thermoelectric figure of merit *zT* ($zT = S^2\sigma T/k$) was estimated

on the basis of the measurement of all the involved transport properties. Overall, the sintered sample was found to have the highest zT in the whole investigated temperature range because of the higher S, σ, and of the lower k. The annealed specimen exhibited larger values of S and σ than the As cast sample as a consequence of the χ_{Co} increase induced by the heat treatment; however, the higher value of thermal conductivity, due the coarser microstructure with respect to the sintered sample, causes a decrease of the thermoelectric conversion efficiency. At last, the As cast specimen was found to have the lowest figure of merit, because of the lowest S and σ values and the largest value of thermal conductivity, due to the more defective structure (i.e. lowest χ_{Co}) and the coarser microstructure, respectively. At 300 K, similar values of zT ($\sim 0.75{\cdot}10^{-3}$) were found for all the samples, while, at 800 K, zT values of $2.18{\cdot}10^{-2}$, $2.52{\cdot}10^{-2}$, and $3.39{\cdot}10^{-2}$ were observed for the As cast, Annealed, and SPS samples, respectively. Such performance is lower than the those of the most promising thermoelectric materials by at least one order of magnitude; however, it should be noted that the main application of Co-based Heusler alloys is not waste heat recovery or energy harvesting.

3.4. Magnetic properties

The magnetization curves $M(H)$ measured at 20 K on the As cast, Annealed, and SPS Co_2ZrSn samples are shown in Fig. 9(a). All $M(H)$ curves exhibit a small hysteresis (coercive fields of the order of 3–4 Oe).

The magnetization at 20 K was found to increase as a function of χ_{Co}, being 1.39 μ_B, 1.59 μ_B, and 1.81 μ_B for the As cast, Annealed and SPS samples, respectively. The magnetization of a pure Co_3Sn_2 sample at the same temperature is also shown for comparison. Considering the low amount of such a secondary phase in the measured Co_2ZrSn samples, it can be safely concluded that the contribution to the overall magnetic signal of the Co_3Sn_2 phase is negligible. Therefore, the values of the saturation magnetization of all Co_2ZrSn specimens can be referred as related to the Heusler compound only. These results are in agreement with previous findings by Kushwaha et al. [43], stating that in Co_2ZrSn, Co-site occupancy has a dramatic effect on the magnetic properties. In particular, the increase of vacancies concentration was found to significantly lower the saturation magnetization, as shown in Fig. 9(a). Considering the magnetic moment at low temperature exhibited by the various samples, it can be noted how such value is related to the Co

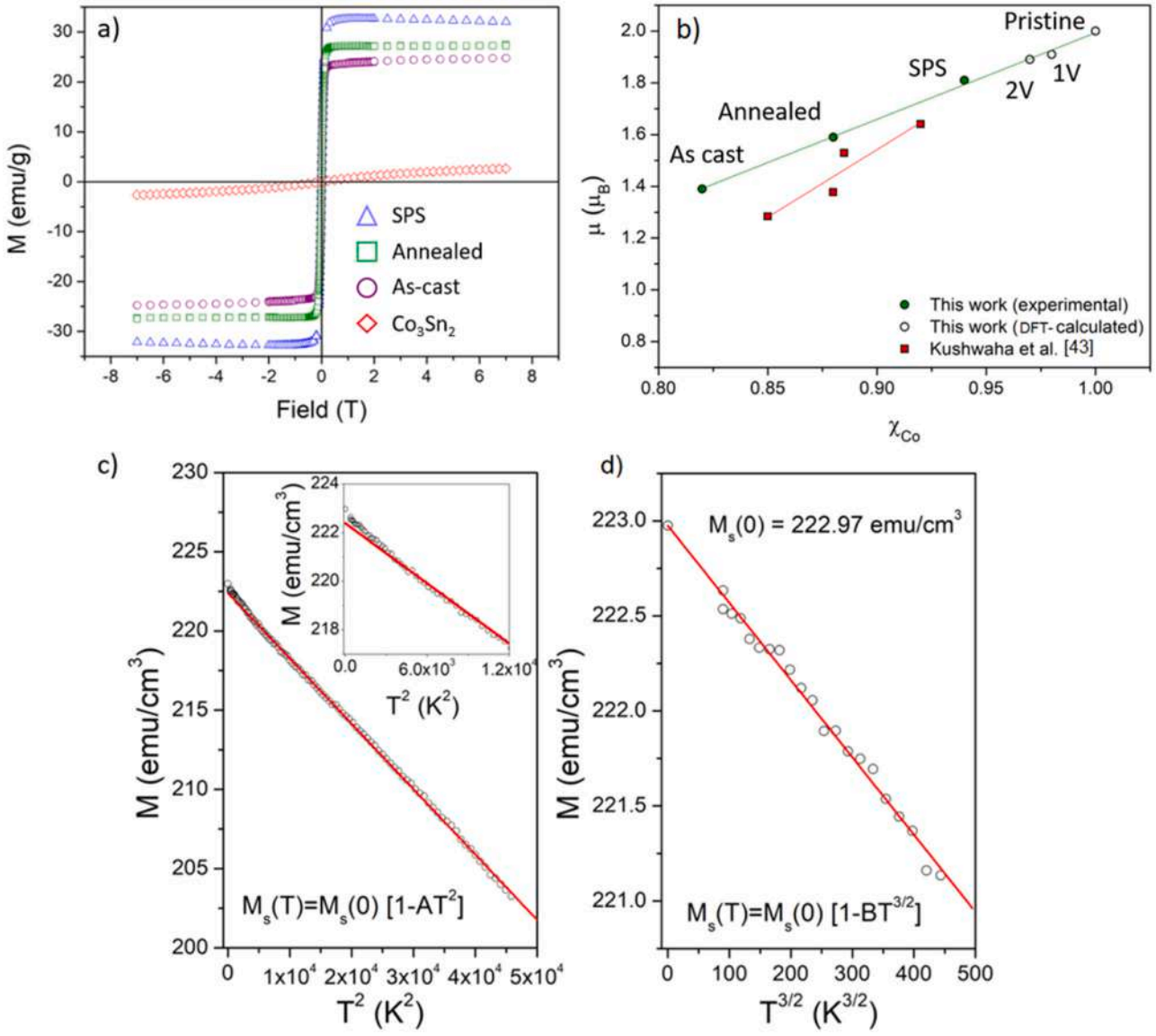

Fig. 9. Hysteresis curves at 20 K of As cast, Annealed, SPS Co_2ZrSn samples, and pure Co_3Sn_2 phase (a). Saturation magnetization as a function of Co-occupancy of Co_2ZrSn (b). Spontaneous magnetization as a function of T^2 (c) and $T^{3/2}$ (d). Inset of (c) shows the deviation from T^2 regime.

occupancy. As highlighted in Fig. 9(b), the dependency of μ on χ_{Co} is linear and qualitatively agrees with the results reported by Kushwaha et al. [43] This confirms that the magnetic moment is mainly located on Co atoms, as suggested by ab-initio calculations [30].

The Annealed sample, which is the closest to the thermodynamic stability due to the extended heat treatment, was selected for further investigations. The low and high temperature magnetic properties were measured respectively with SQUID and VSM, allowing to obtain a complete magnetization curve as a function of temperature (Figure S10 of Supplementary Material) under a constant field of 5 kOe (this value has been selected in order to avoid spurious effects on magnetization related to the presence of magnetic domains). The curves obtained using the two instruments match satisfactorily. The overall behavior of the M (T) shows the degradation of magnetic order by effect of the increasing temperature and allows to get an estimation of the Curie temperature. However, the presence of a constant applied field smears out the transition region. The Curie temperature more accurately derived by the Arrott plot method [30] and was estimated to be 448 K, which is close to the previously measured value of 454 K [30]. The behavior of magnetization at low temperatures was found to be accurately fitted by the expression $M_s = M_s(0)(1 - AT^2)$, where M_s is the spontaneous magnetization of the compound. This quantity is adequately represented by the experimental value taken at 5 kOe, which is sufficient to remove all magnetic domains, bringing the sample close to magnetic saturation and A the slope of the fitted red line, as shown in Fig. 9(c). Such a quadratic law holds up to more than 200 K. At the lowest temperatures however, the $M \propto T^2$ curve was found to deviate upwards, as shown in the inset of Fig. 9(c), making the previous law unsuitable for the description of the magnetization for $T \rightarrow 0$ K. This deviation starts to occur at approximately 58 K. Below such a temperature, the magnetization is instead best fitted by the Bloch law $M_x(T) = M_s(0)(1 - BT^{3/2})$, indicating Bloch-type localized magnetism, as shown in Fig. 9(d), with B the slope of the fitted red line. This result is similar to the one reported in a previous work [30], and is coherent with the trends of electrical resistivity presented in Fig. 7(d). In fact, as already demonstrated for other Heusler compounds [30,35,62,68], such a crossover from a low-T, Bloch-type localized magnetism to a high-T Stoner-type itinerant magnetism can be linked to a crossover from a half-metallic state (where collective spin-wave excitations predominate) to a conductive ferromagnetic state (where the decay of magnetization is caused also by spin fluctuations), as already discussed for σ. The crossover temperature of 58 K determined here is also coherent with that of 64 K, independently assessed by the electrical resistivity measurements, as shown in Fig. 7(d).

From Fig. 9(a) it had been possible to conclude that the effect of the secondary phase Co_3Sn_2 on magnetization intensity of specimens is negligible. The effect on the direction of magnetization was studied by Magnetic Force Microscopy (MFM). The magnetic domain configuration of the Annealed sample is shown in Figure S11(a) (Supplementary Material). The sample is measured at the remanence state that is reached after the application of a saturating magnetic field along the sample plane. The MFM image displays a distinctive domain configuration, wherein a uniform contrast is observed in the Co_2ZrSn phase, while a black-and-white striped pattern emerges in the proximity of Co_3Sn_2 inclusions. This suggests that the magnetisation predominantly aligned in the sample plane within the Co_2ZrSn phase is forced to tilt off by the inclusions, resulting in a perpendicular component of magnetisation, as evidenced by a change in contrast in the image. In Figure S11(b), the same portion of the sample is investigated by MFM under a magnetic field of 600 Oe applied along the sample plane. As a result, the black-and-white striped pattern has almost completely disappeared, and a more homogeneous contrast is evident. This occurs because the applied field rotates the perpendicular component of magnetisation in the sample plane, thereby reducing the observed contrast in the image.

3.5. Ab-initio calculations

The electronic band structure and density of states of pristine Co_2ZrSn are shown in Fig. 10(a). The alloy shows a half-metallic band gap in the minority-spin band and a conductive majority-spin band. A magnetic moment of 2.0 μ_B per formula unit was obtained, being also almost exclusively determined by Co atoms, as well as the density of states in proximity of the Fermi level. The band gap energy (E_G) is in this case 0.37 eV, while the spin-flip energy E_{flip}, defined as the difference between the energy of the lower limit of the minority-spin conduction band and the Fermi energy (E_F), is equal to 0.18 eV.

The transport properties of Co_2ZrSn were simulated on the defect-free system from 10 K to T_C, since above the Curie point the simulation is not reliable, because the density of states changes as a result of the paramagnetic transition. A charge carrier concentration equal to $1{\cdot}10^{28}$ m^{-3} was arbitrary chosen coherently with the experimentally observed conductive metallic behavior, Fig. 7(d). In Fig. 10(b), it can be noted how the Seebeck coefficient is negative and linearly increase in absolute value as a function of temperature. At 10 K, pristine Co_2ZrSn exhibits a S value of -2.25 μV K^{-1}, while at 300 K this is -10.34 μV K^{-1} which is close to the experimental ones (approximately -9 μV K^{-1}). The electrical conductivity and the electronic contribution to the thermal conductivity (k_{el}) divided by the relaxation time were also calculated, both presenting trends which are qualitatively consistent with the experimental results, as shown in Figs. 10(c) and 10(d). At 300 K, the calculated figure of merit ($4.55{\cdot}10^{-3}$), Fig. 10(e), was found to be larger than the experimental value ($0.75{\cdot}10^{-3}$) likely due to the underestimation of the thermal conductivity in the computation where the lattice contribution was not taken in account. The Hall coefficient was also calculated (see Figure S12 of Supplementary Material), being at 10 and 300 K equal to $5.98{\cdot}10^{-10}$ and $5.58{\cdot}10^{-10}$ m^3 C^{-1}, respectively. Overall, these trends found for Co_2ZrSn are comparable with those previously reported for the Co_2HfSn Hesuler compound [32].

Having experimental evidence of a linear trend of magnetic moment as a function of χ_{Co}, two different concentrations of the Co vacancy defect were investigated. From a 128-atoms supercell, one and two Co atoms were removed obtaining the 1 V and 2 V systems, which have $Co_{1.97}ZrSn$ ($\chi_{Co} = 0.984$) and $Co_{1.94}ZrSn$ ($\chi_{Co} = 0.969$) formula unit, respectively. In the 2 V system, the two vacancies were located as fourth nearest-neighbours relative to each other. The band structure and DOS of 1 V and 2 V are shown in Fig. 11. ΔE_{form} is endothermic by only 0.001 eV and by 0.007 eV for 1V and 2V, respectively, which correspond to a temperature of approximately 11 K and 81 K, respectively. Hence, Co vacancy is predicted to be an extremely likely defect also in Co_2ZrSn, as already at 11 K the defect is thermodynamically stable. Being the effective stoichiometry of the 1 V and 2 V systems extremely similar, their formation energies were also found to be approximately the same with respect to the pristine compound. Fig. 11, showing the band structure and DOS of the 1 V and 2 V defective structures, reveals that the progressive introduction of vacancies, at least for the concentrations considered here, does not cause the appearance of energy states inside the minority-spin band gap, conserving the half-metallicity of the system. At the same time, the calculated band gap energies progressively decrease (0.35 eV for $Co_{1.97}ZrSn$, 1 V, and 0.33 eV for $Co_{1.94}ZrSn$, 2 V) as the concentration of vacancies inside the supercell grows. Interestingly, E_{flip} remained constant at 0.18 eV for both the defective supercell, showing the same value of the pristine compound. This suggests that in defective systems it is the valence band which shifts towards the Fermi level, while the conduction band remains at the same distance from E_F as in the pristine material. The decrease of the band gap energy when increasing the vacancy concentration agrees with the corresponding decrease of the Seebeck coefficient observed experimentally.

In Table 4, the values of lattice parameters, Co occupancy, and magnetic moment of the studied systems (both calculated and experimental) are collected. The mutual relationships between such quantities are reported in Figs. 3(a) and 9(b). The dependency of the lattice

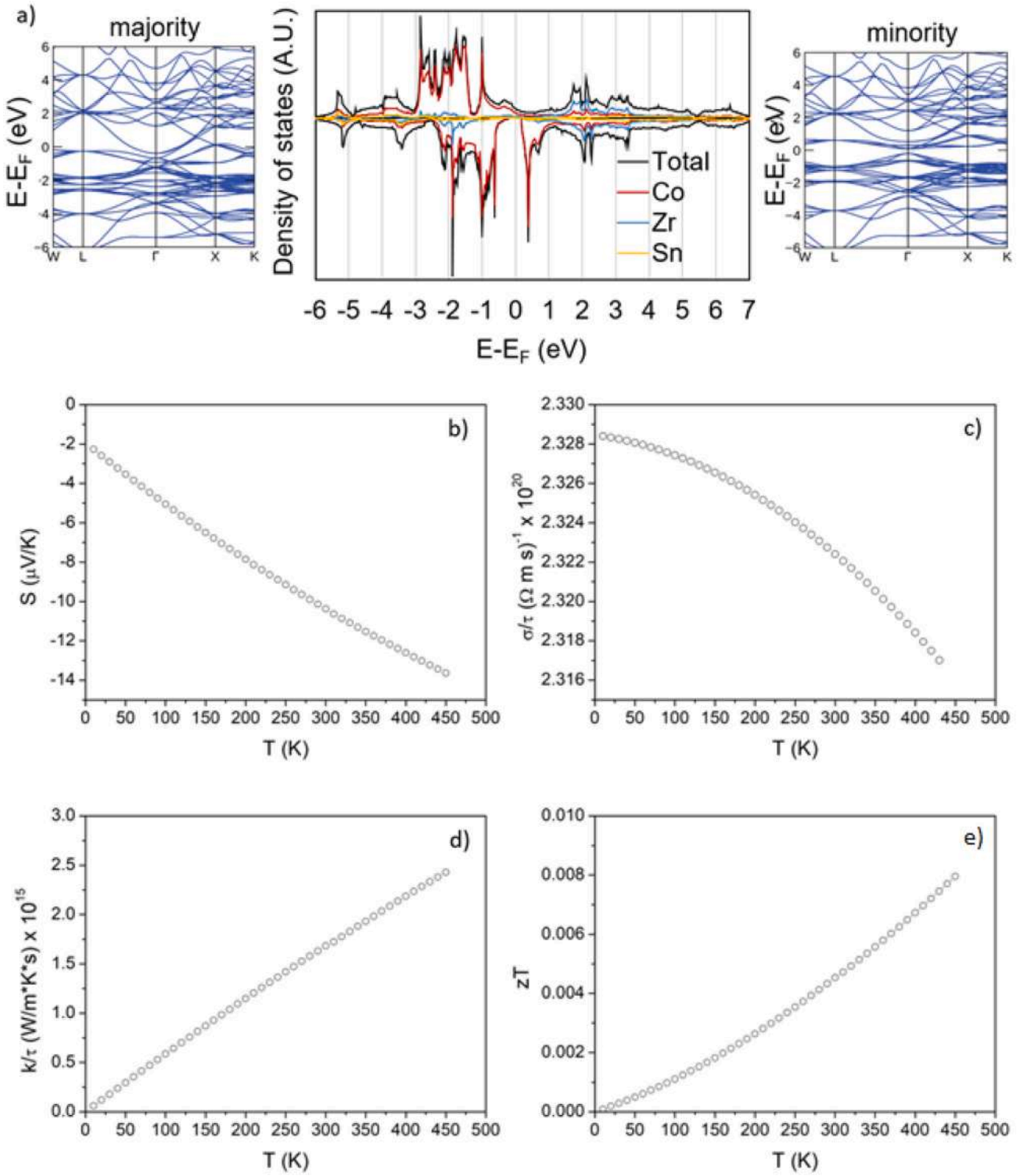

Fig. 10. Electronic band structure and density of states (a), Seebeck coefficient (b), electrical conductivity (c), electronic thermal conductivity (d), figure of merit zT (e) calculated for the pristine Co_2ZrSn.

parameter from χ_{Co} is linear for both the simulated and measured systems (Fig. 3a). Such two trends are in qualitative agreement; however, they do not quantitatively match, as the results of calculations is highly dependent on the computation parameters (cutoff energy, convergence algorithm, k-points grid etc.), functional (PBE, PBEsol, Hartee-Fock, hybrids, etc.) and methodology (PAW, LAPW, Thomas-Fermi etc.). The observed trend can be also due to the lattice thermal expansion, as experimental *a* values are collected at room temperature (RT), while those calculated are to be referred at absolute zero. Interestingly, our calculated data are in optimal agreement with the trend defined by single crystal measurements in the literature [43]. This is plausible as DFT calculations are performed on infinite crystals; thus, experimental data obtained from single crystal measurements represent more closely the ideal conditions used in ab-initio simulations.

Most importantly, the trend of magnetic moment as a function of Co occupancy is the same for experimental and calculated Co_2ZrSn, Fig. 9

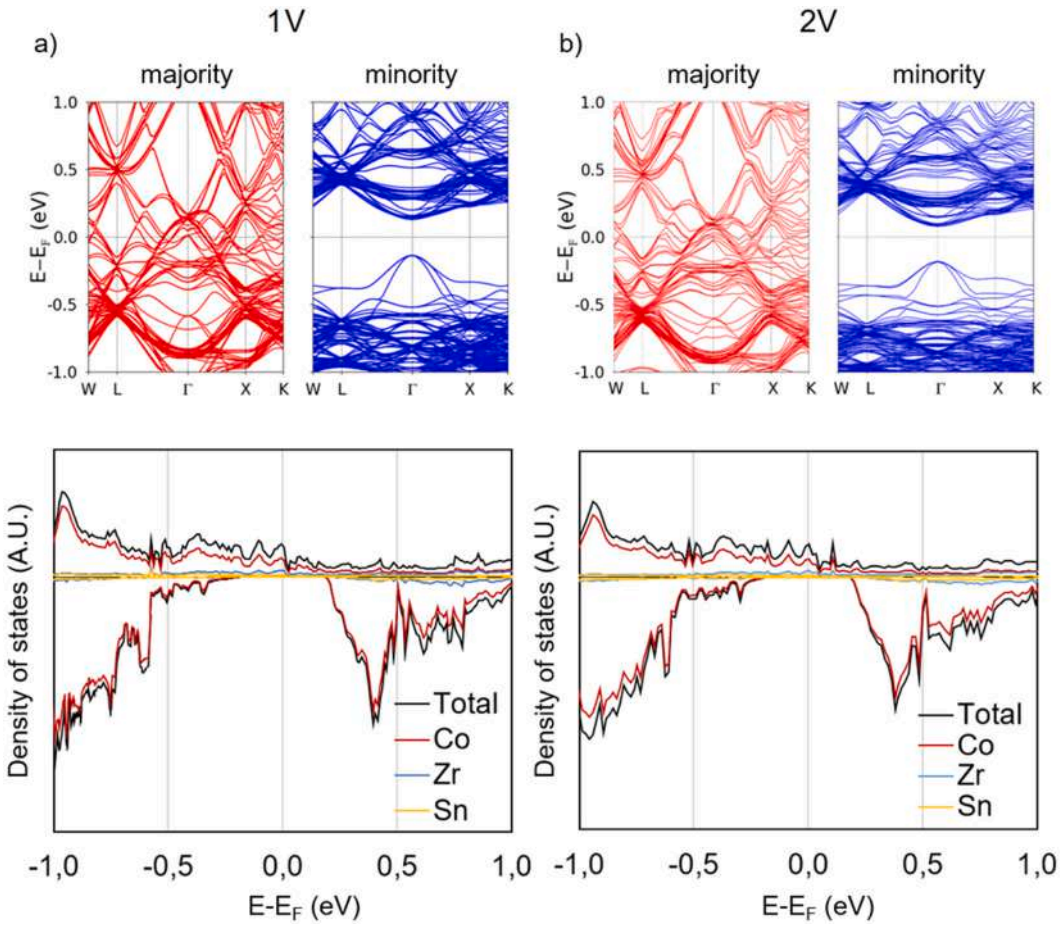

Fig. 11. Band structure and density of states in proximity of the Fermi level of 1 V (a) and 2 V systems (b).

Table 4
Computed values of the lattice parameter (a), the Co-site occupancy (χ_{Co}), the band gap energy (E_g), spin flip energy (E_{flip}), magnetic moment (M) and formation enthalpy of vacancies for the pristine and defective structures. The defect formation energy was calculated with respect to the pristine compound and normalized for defect concentration. Experimental values of the lattice parameter (a), the Co-site occupancy (χ_{Co}) and magnetic moment (M) for samples processed by different techniques.

Sample	a (Å)	χ_{Co}	E_g (eV)	E_{flip} (eV)	M (μ_B)	ΔE_{form} (eV)
Pristine	6.287	1	0.37	0.18	2.00	-
V	6.280	0.98	0.35	0.18	1.91	0.001
2 V	6.274	0.97	0.33	0.18	1.89	0.007
SPS	6.3028	0.94	-	-	1.81	-
Annealed	6.2448	0.88	-	-	1.59	-
As cast	6.2225	0.82	-	-	1.39	-

(b). Such quantitative agreement allows us to make the following considerations. First, the selected set of computational parameters is highly reliable in estimating the magnetic properties of the Co_2ZrSn compound as a function of Co occupancy. Second, in real samples, the magnetic moment is almost exclusively located on Co atoms, as predicted by computations. Last, Co vacancies are responsible for a linear decrease of the magnetic moment as a function of their concentration in the system. From simulations, this do not coincide with a loss of half-metallicity. The strong agreement between computed and measured values, both from this work and from those reported by Kushwaha et al. [43], both for single crystals and polycrystalline Co_2ZrSn, strongly suggests that this is the case also in actual samples. Overall, the change in the DOS of real alloys as a function of temperature is difficultly deducible from DFT calculation, which are performed at 0 K; nevertheless, the experimental evidence of low-*T* scattering mechanisms compatible with half-metallic systems, and the rather good agreement with simulations strongly support the indication of half-metallicity, which is however highly susceptible to defects and lattice disorder.

As stated in 3.1, the linear decrease of the lattice parameter with the decreasing χ_{Co} is incompatible with the assumption of Zr and Sn antisites defects involving the 8c position, as both Zr and Sn have larger atomic radius than Co. Such qualitative argument was investigated by calculating the effect of several other defects involving the 8c site on the lattice parameter of Co_2ZrSn. Using the same 2x2x2 supercell used for vacancies, the following defects were calculated.

- Zr anti-site: the substitution of one Co atom with one Zr atom.
- Sn anti-site: the substitution of one Co atom with one Sn atom.
- Co/Zr swap: the mutual position exchange of one Co atom with one first-neighbouring Zr atom.
- Co/Sn swap: the mutual position exchange of one Co atom with one first-neighbouring Sn atom.
- Off-stoichiometry: as explained in the previous sections, Co_2ZrSn was experimentally found, in its most stable form (see annealed sample) in a composition different from the theoretical 50 % Co, 25 % Zr, 25 % Sn (at%) per formula unit. In real samples, the stoichiometry of the Heusler phase is approximately 48 % Co, 26 % Zr, 26 % Sn. This stoichiometry was recreated in 128-atoms supercells combining an Zr anti-site and a Sn anti-site defect replacing Co atoms, resulting in an empirical $Co_{1.88}XSn$ formula unit. The effect of configurational entropy was also considered. A first defect, named Type 1, was obtained by replacing Co atoms in the (0.375; 0.375; 0.375) and (0.625; 0.625; 0.375) fractional coordinates, which are

separated by a relatively close distance equal to $\frac{1}{4}a\sqrt{3}$. Type 2 defect was instead obtained by replacing Co atoms located in the (0.125; 0.125; 0.875) and (0.625; 0.625; 0.375) sites, being separated by a farther $\frac{1}{2}a\sqrt{3}$ distance.

A summary of the lattice parameters and formation energies of such investigated defects is presented in Table 5. It is possible to note that the lowest formation energy was found for vacancy defects, which formation is endothermic by only 0.001 eV (or 11 equivalent K). All other defects present formation energies higher than that of Co vacancy. Second, as expected, all the calculated defects, with the exception of Co vacancies, lead to an increase of the lattice parameter with respect to the pristine compound, leaving the Co vacancy the only defect involving the 8c site to be able to cause the experimentally observed shrinking. Such evidence, together with the observations of I(200)/I(220) and of the Rietveld refinements, reasonably exclude that the measured experimental trends are caused by any other defect except Co vacancy. This behaviour is different from that of Fe-based Heusler alloys, where antisite related disorder is reported to be the most important [45,72], leading to phenomena like spin-fluctuations and Kondo effect [73].

The phonon band structure and density of states of the pristine Co_2ZrSn compound are reported in Fig. 12. Among the 48 total modes, it is possible to note from the phonon dispersion diagram, Fig. 12(a), that the lowest frequency vibration approach 0 THz at the Γ point. These are acoustic modes, which consist of in-phase oscillation of all atoms and are composed by one longitudinal and two transverse modes. The two transverse modes are degenerate from W to L to Γ. At higher frequencies are located the optical modes, 45 in total, consisting in out-of-phase vibrations of the atoms in the supercell. It is possible to note that, in the region between 0 and 3 THz, a significant overlap between the acoustic and optic modes occurs in each investigated k-point, with the exception of Γ. This high extent of overlap is present also between optical-optical modes in the higher region of the diagram. Finally, a small band gap of approximately 0.08 THz separates at 5.89 THz the set of higher frequency optical modes. In Fig. 12(b), the phonon density of states (pDOS) is shown. Here, it can be noted how the low frequency vibrations (below 3.8 THz) are dominated by the contribution of Sn atoms, while Co atoms are the main contributors in the middle section (from 3.8 to 5.8 THz). Last, the high frequency optical modes above the band gap are formed prevalently by motions of Zr. Again, a strong similarity with the phonon properties of the Co_2HfSn Heusler compound is present [32].

The thermal properties in the harmonic approximation were also calculated, and they are shown in Fig. 12(c). The Helmoltz free energy (red) present a decreasing trend as a function of temperature, having a value of 11.35 kJ mol^{-1} at 0 K. This indicates that atomic oscillations are predicted to occur also at absolute zero giving a phonon contribution. On the other hand, entropy (blue) was expectedly found to increase with the increasing T. Last, the heat capacity at constant volume, C_V (green), follows at low temperatures the Debye model, reaching at higher T a plateau. Having 4 atoms in the formula unit, the heat capacity should approach a value of 12 R, or 99.7 J mol^{-1} K^{-1}. The calculated C_V at 1000 K is 99.3 J mol^{-1} K^{-1}, in good agreement with the theoretical. A comparison with the experimental value 159.96 J mol^{-1} K^{-1} obtained from 323 K to 673 K (see Section 2.3) shows however that the calculated value, being obtained in the harmonic approximation, does not take into account anharmonic contributions, that most probably take place in the sample already at 323 K.

Thermal conductivity's lattice contribution was estimated according to the Slack's model [74]:

$$k_{lat} = 3.1{\cdot}10^{-6}\frac{m\theta_D\delta}{\gamma^2 N^{2/3}T} \quad (7)$$

where θ_D is the Debye temperature in K, δ is the cubic root of the cell volume in Å^3, N is the number of atoms in the primitive unit cell, m is the average atomic mass in atomic unit, and γ the Grüneisen parameter. θ_D and γ have been derived from the longitudinal and transverse sound velocities calculated from the elastic moduli. A detailed explanation on the calculation methods used to estimate all the above mentioned contributions to k_{lat} has been already provided in Ref. [32] (where the same model was applied to the Co_2HfSn alloy), and detailed in the Supporting Information as well.

The calculated elastic and thermal properties of pristine Co_2ZrSn are summarized in Table 6. These values are in good agreement both with those previously reported for this same compound [75], and they are also very similar to those found for the Co_2HfSn Heusler alloy [32].

Comparing Table 6 with Fig. 8(c), it can be seen how the k_{lat} calculated at 400 K significantly differs from the experimental value measured at the same temperature. As previously highlighted for the similar Co_2HfSn compound [32], such discrepancy arises from the assumptions on which the Slack's model is based. First, it is to be reminded that k_{lat} tends to be systematically overestimated up to one order of magnitude when the relative atomic mass of the elements constituting the alloy is larger than 100 % [76]. Secondly, for compounds in which the acoustic and optical phonon modes strongly overlap like in the present case (see Fig. 12), the model is expected to produce inaccurate results since it is not possible to integrate the acoustic and optical contributions separately [74]. Also, this model neglects all the scattering phenomena besides those between acoustic phonons. This means that scattering mechanisms occurring at grain boundaries, with impurities, vacancies, dislocations etc. are not taken into account [74,76]. In order to mitigate these limitations, an important prescription proposed by Slack is to evaluate k_{lat} at temperatures sufficiently larger than θ_D [74]. Being θ_D and T_C extremely close, this request cannot be fulfilled, as the DFT calculations have been performed at 0 K in the ferromagnetic state. Neglecting this issue, a k_{lat} of 16.2 Wm^{-1}K^{-1} is obtained at 800 K, which is closer to the experimental value with respect to the one calculated at 400 K (table 6). Comparable results were obtained for various other semiconductive Heusler compounds [76]. A correction to the Slack's model proposed by Domb and Salter [77] has been already quite successfully applied to Co_2HfSn [32]. Here, a new Debye temperature θ'_D is defined for face centered cubic structures as in Eq. 8 in order to take into account the overlap between the acoustic and phonon branches:

$$\theta'_D = \frac{h\nu_{MAX}}{k_B}\sqrt{\frac{5I(2)}{3}} = \frac{h\nu_{MAX}}{k_B}\sqrt{\frac{5}{6}} = 0.9129\frac{h\nu_{MAX}}{k_B} \quad (8)$$

with h and k_B are the Planck and Boltzmann constants, and ν_{MAX} the maximum frequency of the phonon spectrum defined in terms of force constants. More detailed information is provided both in Refs. [32,77] and in the Supplementary Material. As ν_{MAX} is in this case 6.6 THz, θ'_D is 285 K. Using θ'_D in Eq. 7, k_{lat} becomes equal to 12.51 W m^{-1} K^{-1} at 400 K. Assuming the density of states being valid even above T_C (e.g. see Ref. [75]), k_{lat} is 6.67 W m^{-1} K^{-1} at 800 K. This value is definitely closer to those obtained experimentally, as reported in Fig. 8(c). It is also worth mentioning that the Slack's model does not take into account the contribution of magnons on lattice thermal conductivity, being then unsuitable for comparisons below T_C.

Overall, both electronic and phonon-related calculations gave results

Table 5
Collection of computed data of lattice parameter (a), magnetic moment at 0 K (M) and defect formation energy (ΔE_{form}) on defective Co_2ZrSn systems. The defect formation energy was calculated with respect to the pristine compound and normalized for defect concentration.

	Zr antisite	Sn antisite	Co/Zr swap	Co/Sn swap	Type 1	Type 2
a (Å)	6.302	6.303	6.294	6.294	6.318	6.318
M (μ_B)	2.00	2.00	1.89	2.00	2.00	1.87
ΔE_{form} (eV)	0.060	0.083	0.112	0.105	0.150	0.149

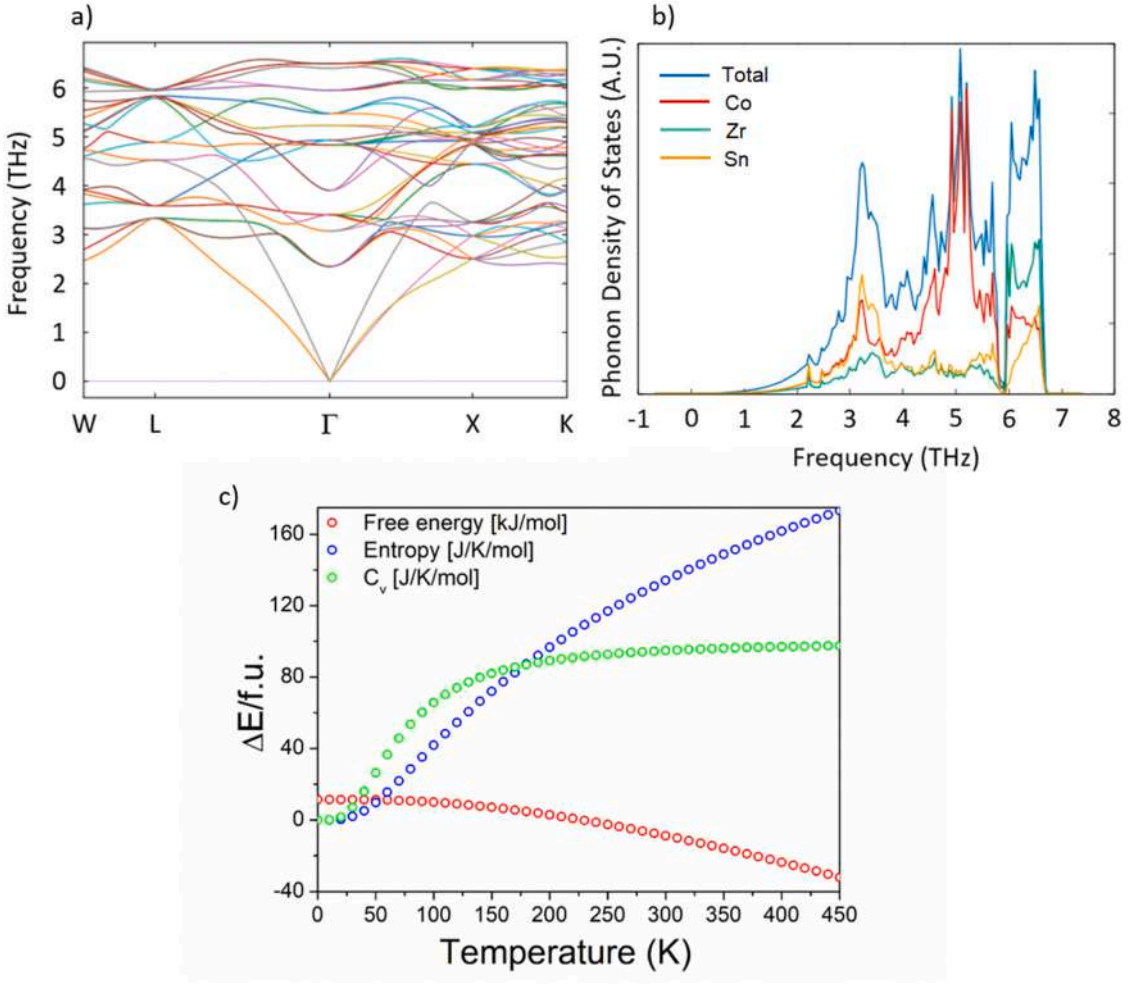

Fig. 12. Phonon band structure (a), phonon density of states (b) and thermal properties (c) of pristine Co_2ZrSn.

Table 6
Calculated elastic constants (C), bulk (B), shear (G) and Young (E) elastic moduli, Debye temperature (θ_D), Grüneisen parameter (γ), and lattice thermal conductivity (k_{lat}) of pristine Co_2ZrSn at 400 K. See Supplementary Material for details.

C_{11}-C_{12} (GPa)	C_{44} (GPa)	G_V (GPa)	G_R (GPa)	G (GPa)
126	87	78	76	77
B (GPa)	**E (GPa)**	**θ_D (K)**	**γ**	**k_{lat} (W $m^{-1}K^{-1}$)**
154	197	391	1.69	32.3

in good agreement with experimental values. The calculated properties of the defective systems (1 V and 2 V) are as well in quantitative agreement with the trends obtained experimentally.

4. Conclusions

In this work we extensively studied the effect of the Co vacancy defect on the structural, transport, and magnetic properties of the Co_2ZrSn compound combining experimental measurements and ab-initio calculations. Samples with various concentrations of point defects (i.e. vacancies) were obtained by different processing methods (arc melting, annealing, melt spinning, SPS), each involving diverse cooling rate and thermal treatments. Such samples were characterized by XRD followed by the Rietveld analysis of the measured patterns, allowing to quantify the amount of vacancies in every specimen by fitting the Co-site occupancy in the structure. The degree of structural disorder in the Co sub-lattice was independently estimated by measuring the intensities of the (200) and (220) XRD reflections, leading to a trend which is coherent with that obtained with the Rietveld refinement. Overall, the lattice parameter was found to linearly decrease with the increasing of Co vacancy concentration, as well as the order of the Co sub-lattice. The effect of processing on the microstructure was evaluated by SEM-EDS and EBSD analysis. The rapid solidification and sintering route were found to be the most effective in refining the microstructure as well as in minimizing the vacancy concentration and, consequently, enlarging the stability field of the Heusler phase. This allowed the preparation of samples with an amount of secondary phases below the XRD detection limit.

The Seebeck coefficients were generally found to follow the trend of Co-site occupancy, with the specimens with higher χ_{Co} presenting the highest values of S. The electrical conductivity was found to depend both on vacancy concentration and grain boundary concentration. Grain boundary scattering is dominant at lower temperature, while at higher temperature the role of the Co-site occupancy prevails. The trend of the electrical resistivity at low temperature (below 300 K) showed a change of regime in proximity of 50–70 K. Below such temperature, the electrical resistivity is proportional to T^2 for all the samples; whereas, at higher T, a T^x ($1 < x < 5/3$) proportionality was observed. In Heusler compounds, this behaviour was found to be not incompatible with a crossover from a low-T half-metallicity to a high-T conductive ferromagnetic state, as the spin-flip electron diffusion is hindered by the half-metallic gap at low temperatures. The thermal conductivity and the

thermoelectric figure of merit zT were experimentally quantified for the various samples. The first was found to be sensitive to microstructure refinement. The second revealed to be mainly sensitive to Co-site occupancy, as the samples with the lowest amount of defects (and highest ordering) presented progressively higher zT. The values of the magnetic moment showed a linear dependency on χ_{Co}. A crossover from a low-T half-metallic to a high-T conductive state was found by measuring the magnetization as a function of temperature. As already reported in previous studies for similar Heusler alloys [30,35], this is the result of spin-flip fluctuations being impossible in systems where half-metallicity is present. The crossover temperature was found to be consistent with those obtained by the measurement of electrical conductivities.

The transport and phonon properties were calculated by DFT for the pristine compound. Assuming an arbitrary carrier concentration of $1{\cdot}10^{28}$ m^{-3}, compatible with the observed conductive behavior, the calculated transport properties are in agreement with the measured ones. The effect of the introduction of vacancy defects in a pristine supercell on the electronic and structural properties of Co_2ZrSn was also investigated. The Co vacancy was found to exhibit a very small formation energy of 11 K, indicating that such defect can easily be formed. Both experiments and calculations show that half-metallicity was not affected by the presence of vacancies, underlining the robustness of this ground state. Nonetheless, a shrinking of the minority-spin band gap is predicted as the concentration of such defect increases in the material. As a consequence of the removal of Co atoms, the magnetization linearly decreases, following the experimental trend. The good agreement between experimental and calculated values of the magnetic moment, considering that only Co-vacancy defects were taken in account in simulations, suggests that the behavior of Co_2ZrSn is mainly affected by this defect, allowing us to neglect the effect of other possible defects inside the material. Simulations conducted on several other defects involving the 8c site gave outcomes which were incompatible with the experimentally observed trends of lattice parameters, furtherly corroborating the all-vacancy approximation.

The present study clarified the electronic and magnetic properties of Co_2ZrSn, also investigating the effect of defects and crystalline disorder on such properties with a combination of experiments and ab-initio calculations. The methodology used in this work was found to effectively give self-consistent and coherent results and can potentially be applied to the study of similar materials. All the experimental outcomes were successfully rationalized in the framework of already existing physical models, and/or strongly supported by first-principles simulations. As strong evidence of the presence of a half-metallic gap at low temperatures was collected for the bulk material, further developments of this work would be the synthesis of this compound as thin-film with a subsequent direct measurement of the spin-polarization and TMR ratio.

CRediT authorship contribution statement

Alleno Eric: Writing – review & editing, Supervision, Resources, Methodology, Conceptualization. **Allia Paolo:** Writing – review & editing, Supervision, Methodology, Formal analysis, Conceptualization. **Tiberto Paola Maria:** Writing – review & editing, Resources, Funding acquisition. **Barrera Gabriele:** Writing – review & editing, Methodology, Investigation, Data curation. **Villeroy Benjamin:** Writing – review & editing, Resources, Investigation. **Rouleau Olivier:** Writing – review & editing, Resources, Investigation. **Fanciulli Carlo:** Writing – review & editing, Resources, Investigation. **Ferrario Alberto:** Writing – review & editing, Methodology, Investigation, Data curation. **Boldrini Stefano:** Writing – review & editing, Resources, Investigation, Funding acquisition. **Baricco Marcello:** Writing – review & editing, Resources. **Palumbo Mauro:** Writing – review & editing, Supervision, Software, Methodology, Investigation, Conceptualization. **Castellero Alberto:** Writing – review & editing, Supervision, Resources, Methodology, Funding acquisition, Conceptualization. **Difalco Alessandro:** Writing – original draft, Software, Methodology, Investigation, Formal analysis, Data curation, Conceptualization.

Funding

Finanziato dall'Unione europea- Next Generation EU, Missione 4 Componente 1 (CUP D53D23005290006, CUP E53D23005120006, CUP B53D23008530006).

Declaration of Competing Interest

The authors declare that they have no known competing financial interests or personal relationships that could have appeared to influence the work reported in this paper.

Acknowledgements

Authors from Università di Torino acknowledge support from the Project CH4.0 under the MUR program "Dipartimenti di Eccellenza 2023–2027" (CUP: D13C22003520001).

Authors would like to thank the "Centro di Competenza sul Calcolo Scientifico" for the computing time on the OCCAM supercomputer.

Appendix A. Supporting information

Supplementary data associated with this article can be found in the online version at doi:10.1016/j.jallcom.2025.180557.

References

[1] A. Hirohata, H. Sukegawa, H. Yanagihara, I. Žutić, T. Seki, S. Mizukami, R. Swaminathan, Roadmap for emerging materials for spintronic device applications, IEEE Trans. Magn. 51 (2015) 1–11.
[2] A. Hirohata, K. Takanashi, Future perspectives for spintronic devices, J. Phys. D. Appl. Phys. 47 (2014) 193001.
[3] S.H. Kang, K. Lee, Emerging materials and devices in spintronic integrated circuits for energy-smart mobile computing and connectivity, Acta Mater. 61 (2013) 952–973.
[4] Y. Xu, S. Thompson, Spintronic materials and technology, CRC press, 2006.
[5] S.K. Kim, G.S.D. Beach, K.-J. Lee, T. Ono, T. Rasing, H. Yang, Ferrimagnetic spintronics, Nat. Mater. 21 (2022) 24–34.
[6] J. Han, R. Cheng, L. Liu, H. Ohno, S. Fukami, Coherent antiferromagnetic spintronics, Nat. Mater. 22 (2023) 684–695.
[7] S.R. Boona, R.C. Myers, J.P. Heremans, Spin caloritronics, Energy Environ. Sci. 7 (2014) 885–910.
[8] G.E.W. Bauer, E. Saitoh, B.J. Van Wees, Spin caloritronics, Nat. Mater. 11 (2012) 391–399.
[9] H. Yu, S.D. Brechet, J.-P. Ansermet, Spin caloritronics, origin and outlook, Phys. Lett. A. 381 (2017) 825–837.
[10] K. Uchida, S. Takahashi, K. Harii, J. Ieda, W. Koshibae, K. Ando, S. Maekawa, E. Saitoh, Observation of the spin Seebeck effect, Nature 455 (2008) 778–781.
[11] I. Žutić, J. Fabian, S. Das Sarma, Spintronics: fundamentals and applications, Rev. Mod. Phys. 76 (2004) 323.
[12] M. Julliere, Tunneling between ferromagnetic films, Phys. Lett. A. 54 (1975) 225–226.
[13] J.M. MacLaren, X.-G. Zhang, W.H. Butler, Validity of the Julliere model of spin-dependent tunneling, Phys. Rev. B. 56 (1997) 11827.
[14] S. Maekawa, S.O. Valenzuela, E. Saitoh, T. Kimura, Spin current, Oxf. Univ. Press (2017).
[15] A.D. Kent, D.C. Worledge, A new spin on magnetic memories, Nat. Nanotechnol. 10 (2015) 187–191.
[16] S.A. Wolf, D.D. Awschalom, R.A. Buhrman, J.M. Daughton, von S. von Molnár, M. L. Roukes, A.Y. Chtchelkanova, D.M. Treger, Spintronics: a spin-based electronics vision for the future, Science 294 (2001) 1488–1495.
[17] A.B. Cahaya, O.A. Tretiakov, G.E.W. Bauer, Spin Seebeck power conversion, IEEE Trans. Magn. 51 (2015) 1–14.
[18] S. Bosu, Y. Sakuraba, K. Uchida, K. Saito, T. Ota, E. Saitoh, K. Takanashi, Spin Seebeck effect in thin films of the Heusler compound Co_2MnSi, Phys. Rev. B. 83 (2011) 224401.
[19] S. Picozzi, A. Continenza, A.J. Freeman, Role of structural defects on the half-metallic character of Co_2MnGe and Co_2MnSi Heusler alloys, Phys. Rev. B. 69 (2004) 94423.
[20] T. Graf, C. Felser, S.S.P. Parkin, Simple rules for the understanding of Heusler compounds, Prog. Solid State Chem. 39 (2011) 1–50.
[21] D. Beretta, N. Neophytou, J.M. Hodges, M.G. Kanatzidis, D. Narducci, M. Martin-Gonzalez, M. Beekman, B. Balke, G. Cerretti, W. Tremel, others, Thermoelectrics: from history, a window to the future, Mater. Sci. Eng. R. Rep. 138 (2019) 100501.

[22] S. Wurmehl, G.H. Fecher, H.C. Kandpal, V. Ksenofontov, C. Felser, H.-J. Lin, J. Morais, Geometric, electronic, and magnetic structure of Co_2FeSi: Curie temperature and magnetic moment measurements and calculations, Phys. Rev. B. 72 (2005) 184434.

[23] R. Shan, H. Sukegawa, W.H. Wang, M. Kodzuka, T. Furubayashi, T. Ohkubo, S. Mitani, K. Inomata, K. Hono, Demonstration of half-metallicity in fermi-level-tuned Heusler alloy $Co_2FeAl_{0.5}Si_{0.5}$ at room temperature, Phys. Rev. Lett. 102 (2009) 246601.

[24] N.I. Kourov, A.V. Korolev, V.V. Marchenkov, A.V. Lukoyanov, K.A. Belozerova, Magnetic and electrical properties of the half-metallic ferromagnets Co_2CrAl, Phys. Solid State 55 (2013) 977–985.

[25] L. Ritchie, G. Xiao, Y. Ji, T.Y. Chen, C.L. Chien, M. Zhang, J. Chen, Z. Liu, G. Wu, X. X. Zhang, Magnetic, structural, and transport properties of the Heusler alloys Co_2MnSi and NiMnSb, Phys. Rev. B. 68 (2003) 104430.

[26] T. Kanomata, Y. Chieda, K. Endo, H. Okada, M. Nagasako, K. Kobayashi, R. Kainuma, R.Y. Umetsu, H. Takahashi, Y. Furutani, others, Magnetic properties of the half-metallic Heusler alloys Co_2VAl and Co_2VGa under pressure, Phys. Rev. B. 82 (2010) 144415.

[27] J. Kübler, G.H. Fecher, C. Felser, Understanding the trend in the Curie temperatures of Co_2-based Heusler compounds: Ab initio calculations, Phys. Rev. B. 76 (2007) 24414.

[28] J. Barth, G.H. Fecher, B. Balke, T. Graf, A. Shkabko, A. Weidenkaff, P. Klaer, M. Kallmayer, H.J. Elmers, H. Yoshikawa, S. Ueda, K. Kobayashi, C. Felser, Anomalous transport properties of the half-metallic ferromagnets Co_2TiSi, Co_2TiGe and Co_2TiSn, Philos. Trans. R. Soc. A Math. Phys. Eng. Sci. 369 (2011) 3588–3601.

[29] T. Kanomata, Y. Amako, Y. Ida, Y. Adachi, T. Osaki, T. Eto, H. Nishihara, I. Shigeta, S. Imada, M. Doi, Magnetic properties of ferromagnetic Heusler alloy Co_2ZrSn, J. Phys. Chem. Solids 164 (2022) 110635.

[30] A. Difalco, G. Barrera, M. Palumbo, A. Castellero, M. Baricco, P.M. Tiberto, P. Allia, Itinerant magnetism, electronic properties and half-metallicity of Co_2ZrSn and Co_2HfSn Heusler alloys, J. Alloy. Compd. 918 (2022) 165464.

[31] A. Rahman, M.U. Rehman, H. Zhao, W. Liu, J. Wang, Y. Lu, K. Ruan, R. Dai, Z. Wang, X. Tao, others, Itinerant magnetism in the half-metallic Heusler compound Co_2HfSn: Evidence from critical behavior combined with first-principles calculations, Phys. Rev. B. 103 (2021) 94425.

[32] A. Difalco, I.G. Winning, M. Palumbo, M. Baricco, A. Castellero, E. Alleno, Transport properties of Co_2HfSn Heusler alloy obtained by rapid solidification and sintering, Solid State Sci. 149 (2024) 107455.

[33] A. Hirohata, D.C. Lloyd, Heusler alloys for metal spintronics, MRS Bull. 47 (2022) 593–599.

[34] A. Difalco, F. Aversano, S. Boldrini, A. Ferrario, M. Baricco, A. Castellero, Synthesis and Characterization of Thermoelectric Co_2XSn (X = Zr, Hf) Heusler Alloys, Metals 10 (2020) 624.

[35] P. Turban, S. Andrieu, B. Kierren, E. Snoeck, C. Teodorescu, A. Traverse, Growth and characterization of single crystalline NiMnSb thin films and epitaxial NiMnSb/MgO/NiMnSb (001) trilayers, Phys. Rev. B. 65 (2002) 134417.

[36] M. Terada, Y. Fujita, K. Endo, Magnetic properties of the Heusler alloys M_2XSn (M= Co or Ni, X= Zr, Nb or Hf), J. Phys. Soc. Jpn. 36 (1974) 620.

[37] K.R.A. Ziebeck, P.J. Webster, A neutron diffraction and magnetization study of Heusler alloys containing Co and Zr, Hf, V or Nb, J. Phys. Chem. Solids 35 (1974) 1–7.

[38] P.G. Van Engen, K.H.J. Buschow, M. Erman, Magnetic properties and magneto-optical spectroscopy of Heusler alloys based on transition metals and Sn, J. Magn. Magn. Mater. 30 (1983) 374–382.

[39] R.V. Skolozdra, Y.V. Stadnyk, Y.K. Gorelenko, E.E. Terletskaya, Influence of vacancies on the magnetic and electrical properties of Heusler phases Me'Co_2-xSn (Me'= Ti, Zr, Hf), Sov. Phys. Solid State 32 (1990) 1536–1538.

[40] A. Ślebarski, A. Jezierski, M. Neumann, S. Plogmann, Influence of vacancies on the electronic structure of CoZrSn Heusler alloys, Eur. Phys. J. B-Condens. Matter Complex Syst. 12 (1999) 519–523.

[41] A. Yamasaki, S. Imada, R. Arai, H. Utsunomiya, S. Suga, T. Muro, Y. Saitoh, T. Kanomata, S. Ishida, Orbital angular momentum and interpretation of core-absorption magnetic circular dichroism on the band picture in Co-based Heusler alloys Co_2YSn (Y= Ti, Zr, and Nb), Phys. Rev. B. 65 (2002) 104410.

[42] W. Zhang, Z. Qian, Y. Sui, Y. Liu, W. Su, M. Zhang, Z. Liu, G. Liu, G. Wu, Magnetism and Hall effect of the Heusler alloy Co_2ZrSn synthesized by melt-spinning process, J. Magn. Magn. Mater. 299 (2006) 255–259.

[43] S.K. Kushwaha, K. Stolze, Z. Wang, M. Hirschberger, J. Lin, B.A. Bernevig, N. P. Ong, R.J. Cava, Crystal growth and stoichiometry-dependent properties of the ferromagnetic Weyl semimetal $ZrCo_{2-x}Sn$, J. Phys. Condens. Matter 29 (2017) 225702.

[44] N. Ashcroft, N. Mermin, Solid State Physics, Holt-Saunders, 1976.

[45] S. Maier, S. Denis, S. Adam, J.-C. Crivello, J.-M. Joubert, E. Alleno, Order-disorder transitions in the Fe_2VAl Heusler alloy, Acta Mater. 121 (2016) 126–136.

[46] L. Lutterotti, S. Matthies, H.-R. Wenk, MAUD (material analysis using diffraction): a user friendly Java program for Rietveld texture analysis and more, : Proc. Twelfth Int. Conf. Textures Mater. (1999) 1599.

[47] S. Boldrini, A. Famengo, F. Montagner, S. Battiston, S. Fiameni, M. Fabrizio, S. Barison, Test rig for high-temperature thermopower and electrical conductivity measurements, J. Electron. Mater. 42 (2013) 1319–1323.

[48] O. Rouleau, E. Alleno, Measurement system of the Seebeck coefficient or of the electrical resistivity at high temperature, Rev. Sci. Instrum. 84 (2013) 105103.

[49] G. Kresse, J. Furthmüller, Efficient iterative schemes for ab initio total-energy calculations using a plane-wave basis set, Phys. Rev. B. 54 (1996) 11169.

[50] P.E. Blöchl, Projector augmented-wave method, Phys. Rev. B. 50 (1994) 17953.

[51] J.P. Perdew, K. Burke, M. Ernzerhof, Generalized gradient approximation made simple, Phys. Rev. Lett. 77 (1996) 3865.

[52] G. Kresse, D. Joubert, From ultrasoft pseudopotentials to the projector augmented-wave method, Phys. Rev. B. 59 (1999) 1758.

[53] G.K.H. Madsen, J. Carrete, M.J. Verstraete, BoltzTraP2, a program for interpolating band structures and calculating semi-classical transport coefficients, Comput. Phys. Commun. 231 (2018) 140–145.

[54] H.J. Monkhorst, J.D. Pack, Special points for Brillouin-zone integrations, Phys. Rev. B. 13 (1976) 5188.

[55] A. Togo, First-principles phonon calculations with phonopy and phono3py, J. Phys. Soc. Jpn. 92 (2023) 12001.

[56] G. Nolze, W. Kraus, PowderCell 2.0 for windows, Powder Diffr. 13 (1998) 256–259.

[57] R. Mahat, S. Kc, U. Karki, J.Y. Law, V. Franco, I. Galanakis, A. Gupta, P. LeClair, Possible half-metallic behavior of $Co_{2-x}Cr_xFeGe$ Heusler alloys: theory and experiment, Phys. Rev. B. 104 (2021) 14430.

[58] P.J. Webster, Magnetic and chemical order in Heusler alloys containing cobalt and manganese, J. Phys. Chem. Solids 32 (1971) 1221–1231.

[59] B.H. Toby, R factors in Rietveld analysis: how good is good enough? Powder Diffr. 21 (2006) 67–70.

[60] S. Cui, G. Ouyang, T. Ma, C.R. Macziewski, V.I. Levitas, L. Zhou, M.J. Kramer, J. Cui, Thermodynamic and kinetic analysis of the melt spinning process of Fe-6.5 wt% Si alloy, J. Alloy. Compd. 771 (2019) 643–648.

[61] K. Ueda, T. Moriya, Contribution of spin fluctuations to the electrical and thermal resistivities of weakly and nearly ferromagnetic metals, J. Phys. Soc. Jpn. 39 (1975) 605–615.

[62] C. Hordequin, D. Ristoiu, L. Ranno, J. Pierre, On the cross-over from half-metal to normal ferromagnet in NiMnSb, Eur. Phys. J. B-Condens. Matter Complex Syst. 16 (2000) 287–293.

[63] A. Barry, J.M.D. Coey, L. Ranno, K. Ounadjela, Evidence for a gap in the excitation spectrum of CrO_2, J. Appl. Phys. 83 (1998) 7166–7168.

[64] P. Allen, Boltzmann theory and resistivity of metals, Kluwer Int. Ser. Eng. Comput. Sci. (1996) 219–250.

[65] D. Bombor, C.G.F. Blum, O. Volkonskiy, S. Rodan, S. Wurmehl, C. Hess, B. Büchner, Half-metallic ferromagnetism with unexpectedly small spin splitting in the Heusler compound Co_2FeSi, Phys. Rev. Lett. 110 (2013) 66601.

[66] S. Chatterjee, S. Samanta, B. Ghosh, K. Mandal, Half-metallic ferromagnetism and intrinsic anomalous Hall effect in the topological Heusler compound Co_2MnGe, Phys. Rev. B. 108 (2023) 205108.

[67] D. Ristoiu, J.P. Nozieres, L. Ranno, Epitaxial NiMnSb thin films prepared by facing targets sputtering, J. Magn. Magn. Mater. 219 (2000) 97–103.

[68] J. Pierre, R.V. Skolozdra, J. Tobola, S. Kaprzyk, C. Hordequin, M.A. Kouacou, I. Karla, R. Currat, E. Lelievre-Berna, Properties on request in semi-Heusler phases, J. Alloy. Compd. 262 (1997) 101–107.

[69] C. Hu, K. Xia, C. Fu, X. Zhao, T. Zhu, Carrier grain boundary scattering in thermoelectric materials, Energy Environ. Sci. 15 (2022) 1406–1422.

[70] H.-S. Kim, Z.M. Gibbs, Y. Tang, H. Wang, G.J. Snyder, Characterization of Lorenz number with Seebeck coefficient measurement, APL Mater. 3 (2015) 041506.

[71] A. Sood, R. Cheaito, T. Bai, H. Kwon, Y. Wang, C. Li, L. Yates, T. Bougher, S. Graham, M. Asheghi, others, Direct visualization of thermal conductivity suppression due to enhanced phonon scattering near individual grain boundaries, Nano Lett. 18 (2018) 3466–3472.

[72] M.L.C. Buffon, G. Laurita, L. Lamontagne, E.E. Levin, S. Mooraj, D.L. Lloyd, N. White, T.M. Pollock, R. Seshadri, Thermoelectric performance and the role of anti-site disorder in the 24-electron Heusler $TiFe_2Sn$, J. Phys. Condens. Matter 29 (2017) 405702.

[73] T. Naka, K. Sato, M. Taguchi, T. Nakane, F. Ishikawa, Y. Yamada, Y. Takaesu, T. Nakama, A. Matsushita, Ferromagnetic quantum singularities and small pseudogap formation in Heusler type $Fe_{2+x}V_{1-x}Al$, Phys. Rev. B—Condens. Matter Mater. Phys. 85 (2012) 85130.

[74] G.A. Slack, The thermal conductivity of nonmetallic crystals, Solid State Phys. 34 (1979) 1–71.

[75] M.Y. Raiâ, R. Masrour, M. Hamedoun, J. Kharbach, A. Rezzouk, A. Hourmatallah, N. Benzakour, K. Bouslykhane, Stability, magnetic, electronic, elastic, thermodynamic, optical, and thermoelectric properties of Co_2TiSn, Co_2ZrSn and Co_2HfSn Heusler alloys from calculations using generalized gradient approximation techniques, J. Mater. Sci. Mater. Electron 33 (2022) 20229–20256.

[76] C. Barreteau, J.-C. Crivello, J.-M. Joubert, E. Alleno, Optimization of criteria for an efficient screening of new thermoelectric compounds: the tinisi structure-type as a case-study, ACS Comb. Sci. 22 (2020) 813–820.

[77] C. Domb, L. Salter, CIX. The zero point energy and Θ crystals, Lond., Edinb., Dublin Philos. Mag. J. Sci. 43 (1952) 1083–1089.